Solar System Research, Vol. 39, No. 5, 2005, pp. 381–409. Translated from Astronomicheskii Vestnik, Vol. 39, No. 5, 2005, pp. 426–456.

Numerical Modeling of the Largest Terrestrial Meteorite Craters

B. A. Ivanov

Institute for Dynamics of Geospheres, Russian Academy of Sciences, Leninskii pr. 38, Moscow, 117979 Russia

Received December 26, 2004

Abstract—Multi-ring impact basins have been found on the surfaces of almost all planetary bodies in the Solar system with solid crusts. The details of their formation mechanism are still unclear. We present results of our numerical modeling of the formation of the largest known terrestrial impact craters. The geological and geophysical data on these structures accumulated over many decades are used to place constraints on the parameters of available numerical models with a dual purpose: (i) to choose parameters in available mechanical models for the crustal response of planetary bodies to a large impact and (ii) to use numerical modeling to refine the possible range of original diameters and the morphology of partially eroded terrestrial craters. We present numerical modeling results for the Vredefort, Sudbury, Chicxulub, and Popigai impact craters and compare these results with available geological and geophysical information.

INTRODUCTION

The lunar surface has preserved traces of the early evolutionary stage of the terrestrial planets to the present day. The witnesses of this epoch, lunar multi-ring basins, were formed during giant impact events ~3.8 Gyr ago or earlier. Giant impact basins are known to exist on Mercury and Mars. Such structures are observed on Jupiter's and Saturn's satellites. Undoubtedly, such giant structures were also formed at the same time on the early Earth, but active terrestrial tectonics has erased even the traces of these catastrophic impacts. A similar resurfacing also occurred on Venus. On both the Earth and Venus, the diameters (D) of the largest known preserved impact structures are 100–300 km. On Venus, the Mead impact crater is largest ($D \approx 270$ km), and ten craters are more than 100 km in diameter. On the Earth, four craters with diameters of more than 100 km have been found to date: Popigai (Masaitis *et al.*, 1975), Chicxulub, Sudbury, and Vredefort (Grieve and Therriault, 2000).

Following the simple similarity laws (Pike, 1980), the morphological types of impact structures (simple, central peak, peak ring craters and multi-ring basins) on planetary bodies with different gravities g are similar if the product gD is conserved. Such a (fairly approximate) similarity can be explained by the fact that the formation of impact craters depends largely on the ratio of the rock strength Y to the lithostatic pressure in the volume of rocks with diameters of the order of the crater diameter. The characteristic value of this pressure can be estimated as ρgD (Melosh, 1989), where ρ is the rock density. At approximately the same strengths and densities of the rocks constituting the surfaces of planetary bodies with solid crusts, the ratio $Y/\rho gD$ is constant at $gD \approx$ const. The validity of this approach was demonstrated both for the morphology of craters on Mercury, the Moon, the Earth, and Mars (Pike, 1980) and for the depth–diameter relationship of impact craters (McKinnon *et al.*, 1997). In this approximation, terrestrial impact structures with diameters of 100–300 km must be similar to lunar impact structures with a factor of 6 larger diameters (600–1800 km). Of course, there can be no close similarity: layering (e.g., the crust thickness), a temperature gradient, and other target parameters make it difficult to rigorously compare the processes. Nevertheless, many structural features of impact formations on the Earth and the Moon can be analyzed by studying the largest terrestrial meteorite craters as analogues of lunar basins (Grieve and Therriault, 2000).

The goal of this paper is to demonstrate the possibilities for a comparative analysis of well-known structural features of the largest terrestrial impact craters and the results of our numerical modeling of their formation. Since the description of crater geology and numerical modeling are independent tasks, both these subjects are presented briefly, where possible, in an attempt to achieve a balance between the detail of the description and the volume of the publication.

The paper is organized as follows. First, we briefly describe the numerical modeling technique and then consider the Popigai (the largest crater found on the territory of Russia), Chicxulub, and Vredefort impact craters. At the end, we also briefly consider the Sudbury crater, which is probably similar in diameter to the Vredefort crater, but was deformed much more strongly by late tectonic movements. All four impact structures considered here were modified to one degree or another by tectonic deformations, erosion, and sedimentation. Therefore, the discussion of the terrestrial craters is preceded by a brief description of the data on the largest craters of Venus (a planet similar to the Earth in diameter and gravity), which preserved their original structure much better.

0038-0946/05/3905-0381

NUMERICAL MODELING OF IMPACT CRATERING

The numerical (computer) modeling of impact crater formation is technically reduced to solving the standard equations of motion for a continuous compressible medium that express the laws of conservation of mass, momentum, and energy. These equations are solved in a discrete representation of the computational region as a grid of elementary cells. We solve the equations of motion for a continuous medium using the SALEB software package. The original version of the program (called SALE-2D by its authors) was published by the Los Alamos Laboratory in USA (Amsden *et al.*, 1980) as a program for computing the motions of a viscous compressible fluid "at all speeds". Subsequently, Melosh *et al.* (1992) supplemented the program with a description of the elastic stresses in a solid by taking into account the shear and tensile fracture in the Lagrangian version of the program. We supplemented the program with the possibility of describing several materials in each cell and the advection of all variables, including the deviator stresses, in the Eulerian version of the program. We also added a more realistic description of the shear strength of rocks (Ivanov *et al.*, 1997) and the possibility of modeling the temporary reduction in the friction of rocks around the growing crater in the acoustic fluidization (AF) model approximation (for details, see Melosh and Ivanov (1999)). The current version of the description of rock strength properties and the AF model are presented in papers by Collins *et al.* (2004) and Wünnemann and Ivanov (2003). A full description and a user's guide for the SALEB program are currently being prepared for publication. The Lagrangian version of the SALE program with a description of solid materials called SALES-2 is maintained by its authors, G. Collins and H.J. Melosh, and is accessible on the Internet at http://www.lpl.arizona.edu/tekton/sales_2.html (February 2005).

SALE is a two-dimensional program. Cratering problems can be solved with it only for a vertical impact under the assumption of axial symmetry. The typical boundary conditions for the impact problem are as follows: the left (vertical) boundary is the symmetry axis, the lower and right boundaries are rigid, undeformable (all speeds are assumed to be zero), and the upper boundary can be rigid or permeable in one direction (the material crossing the upper boundary leaves the computational region forever). A nonuniform computational grid is used to attenuate the waves reflected from the rigid boundaries. The central zone where the crater is formed is covered with square cells of the same size. Outside the central zone, the cell size is gradually increased to push the rigid boundary as far away as possible. For a typical computation, the central region consists of 200–250 cells in both the horizontal and vertical directions; 50–100 nonuniform cells outside the central region allow the action of the waves reflected from the rigid outer boundaries of the computational region to be delayed and weakened. In physical units, for example, to compute the formation of a crater ~50 km in radius, the central zone has a diameter of the order of (slightly larger than) the expected crater diameter, while the outer boundaries of the computational grid are at a distance of 350–400 km in the horizontal and vertical directions.

An essential component of the numerical modeling of impact processes is the equation of state. The equations of state close the system of equations of motion for a continuous medium by relating the density, pressure, and specific internal energy (or temperature) of the material located in each cell of the computational grid at a given time. During high-velocity impacts, the equations of state must describe the properties of materials from a normal density to three-to-fivefold compression (to reproduce pressures of 100–500 GPa) and then its expansion to densities below the normal one (to the point of a rarefied gas if the material is subjected to decompression vaporization). For each state of the material (liquid, solid, gaseous), there are theoretical models that are substantiated by a detailed comparison with experimental data (see, e.g., the classic monographs and textbooks by Landau and Lifshitz (1951), Zeldovich and Raizer (1966), and Zharkov and Kalinin (1968)). A smooth interpolation between the density and temperature regions described by various models with fitting to the available experimental data is important for numerical modeling. In this paper, we use the ANEOS (ANalytical Equation Of State) code (Thompson and Lauson, 1972) to set up the equations of state for rocks. ANEOS provides a number of options to compute the pressure, temperature, entropy, and other parameters using the Mie–Grüneisen approximation for a solid material with a smooth transition to the Thomas–Fermi model at large compression ratios and to an ideal gas when the material vaporizes.

An essential feature of the ANEOS code is a smooth interpolation between individual models. As in most of the other approaches, here, the expressions for free (Helmholtz) energy F as a function of density ρ and temperature T are primarily interpolated. All of the remaining thermodynamic variables are expressed as the derivatives of F; for example, the pressure $p = \rho^2(\partial F/\partial\rho)$, the entropy $S = -(\partial F/\partial T)$, and the specific internal energy $E = F + TS$.

The free energy F is then represented as the sum of several additive components. The quantity F (and, hence, its derivatives, such as the pressure and the specific internal energy) is the sum of three main parts: the so-called "cold" component, F_c, which depends only on the mean separation between atoms (specified by the value of F at $T = 0$ K), the "thermal" part, F_{th}, which is determined by the thermal vibrations of atoms and molecules, and the "electron" part, F_e, for the range of high temperatures where the material ionization and the electron gas pressure are significant:

$$F = F_c(\rho) + F_{th}(\rho, T) + F_e(\rho, T). \quad (1)$$

Accordingly, the pressure and the specific internal energy can also be represented as the cold, thermal, and electron components:

$$p = p_c(\rho) + p_{th}(\rho, T) + p_e(\rho, T), \quad (2)$$

$$E = E_c(\rho) + E_{th}(\rho, T) + E_e(\rho, T). \quad (3)$$

The "cold" pressure and energy are related by

$$p_c = \rho^2(dE_c/d\rho). \quad (4)$$

For pressures below ~1000 GPa, the electron components are not very important.

The quality of any analytical equations of state depends on the availability of experimental data and the possibility of their best fitting, which depends primarily on the type of models used to set up the equations of state. The authors of ANEOS sought primarily to reproduce well the experimental shock adiabat of the material. In this paper, we use the tables that we constructed using the ANEOS code for granite, quartzite, and dunite, which model the rocks of the terrestrial crust and upper mantle. The original tables of parameters for granite were published by Pierazzo *et al.* (1997) and for quartzite and dunite by Melosh (2000).

In the original form, the ANEOS code has a number of significant limitations:

(1) The solid-state polymorphic phase transitions typical of rocks take complex compression–decompression paths (as, e.g., for the quartz–stishovite transition; see the review article by Kuznetsov (2000)). ANEOS does not reproduce the characteristic hysteresis in the compression–decompression cycle—the polymorphic phase transitions are described as equilibrium ones.

(2) If the option of describing a polymorphic phase transition is set, then the melting of material cannot be described completely (the code computes the smooth transition from a solid material to a two-phase equilibrium curve of the condensed and vaporized states without separating the melt phase). Consequently, the temperatures in the domain of existence of a melt are slightly overestimated, since the melting latent heat is not subtracted from the specific internal energy of the material.

(3) Only one solid-state polymorphic phase transition can be described.

These shortcomings can be largely overcome by computing each phase of the material (solid or liquid) as a separate material with an individual set of input parameters for the ANEOS code followed by the computation of phase equilibrium lines. This work is currently being performed (see Ivanov, 2003b, 2004a, 2005; Ivanov *et al.*, 2004).

IMPACT CRATERS ON VENUS

Before discussing the terrestrial impact structures, it seems pertinent to briefly consider the craters on other planets. For simple craters, the best objects for comparison are numerous lunar craters for which a large body of data has been collected during manned and unmanned flights to the Moon. In contrast to simple bowl-shaped craters, the morphology of complex craters depends on the crater diameter. The morphological sequences of craters on different planets are similar, but morphologically similar craters on planetary bodies with different gravities have different diameters. Therefore, the morphological sequence of impact craters closest to terrestrial craters exists on Venus. The surface of Venus is known to be composed of rocks similar (at least in mechanical properties) to the rocks of the terrestrial crust, oceanic (basalts) (Barsukov, 1992; Surkov and Barsukov, 1985) or continental (Nikolaeva, 1990).

The surface gravity on Venus is only 10% lower than that on the Earth (8.9 versus 9.8 m/s^2). Consequently, one might expect the Venusian craters to be similar to "fresh" terrestrial impact craters of the same diameter immediately after their formation: the erosion rate of the Venusian surface is very low, because the adiabatic atmosphere is almost immovable (near the surface) and because there is no water at a surface temperature of about 500°C. From the standpoint of impact cratering, the strongest effect of a high surface temperature is assumed to be a factor of 10 longer (than under terrestrial conditions) solidification time of the impact melt loaded with clasts in Venusian impact craters (Ivanov *et al.*, 1992). At the same time, the absence of water on the Venusian surface is an important reason for assuming that there is no close similarity in the cratering processes: water changes the mechanical and thermodynamic properties of rocks by affecting significantly, for example, their strengths and melting temperatures. Apart from this, there are no terrestrial-type sedimentary rocks on Venus (except the volcanic and aeolian sediments).

Figure 1 shows radar images of several Venusian impact craters with diameters in the range 100 to 300 km. It is clearly seen that a well-defined crater rim and an inner ring rim inside the crater are typical of this range of diameters.

The first depth measurements for Venusian craters were published by Ivanov (1989) and Ivanov *et al.* (1986). A shifted-image technique was used for small craters. A radar image of the surface was constructed by a computer on a perfect spherical surface. The areas below the level of this sphere prove to be shifted, creating the impression of the absence of concentricity, for example, a shift of the flat floor of the crater relative to its rim. This (wrong) impression can be expressed in the form of formulas that allow the visible image shift into the depth of the crater floor relative to the rim crest to be transformed using the known geometry of operation of a side-looking radar. Since the craters are not perfectly concentric structures, this technique yields mean depths of a group of craters of the same diameter. We emphasize once again that the shifted-image method

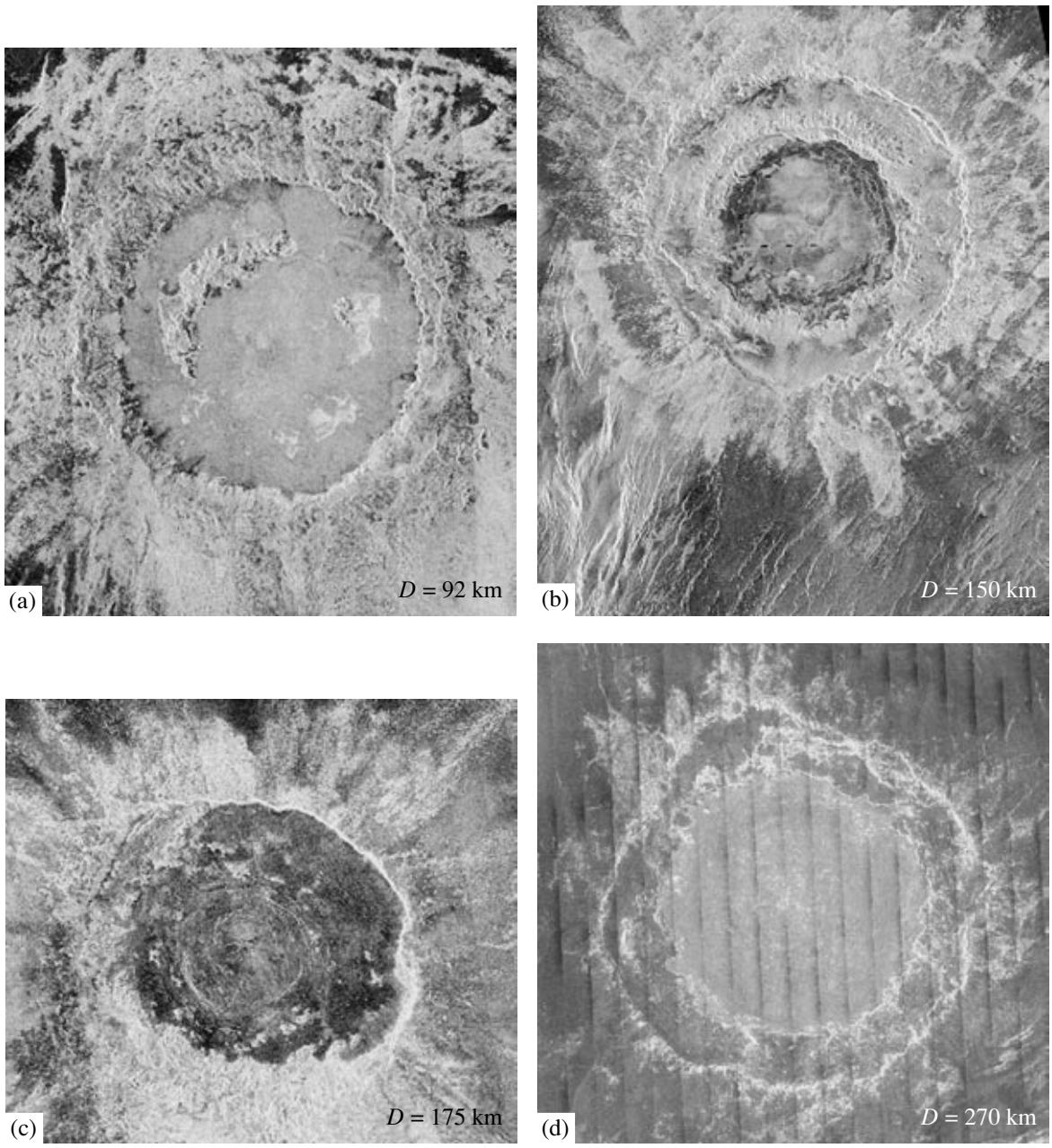

Fig. 1. *Magellan* radar images of four Venusian craters. All craters have complex morphology with a well-defined crater rim and an inner ring uplift. Images from the database of the Lunar–Planetary Institute, Houston, (http://www.lpi.usra.edu/resources/vc/vchome.html), were used: (a) Greenaway, (b) Meitner, (c) Isabella, and (d) Mead. Approximate crater diameters are indicated.

yields only a depth estimate for the floor of a crater relative to the rim crest.

The depths for the largest craters on Venus were measured using radio-altimeter data from the Magellan spacecraft (Ivanov and Ford, 1993). Since the reflection spot of the radio altimeter (~40 km on the Magellan spacecraft) is too large to distinguish the relatively narrow crater wall, the crater depth measurements relative to the level of the surrounding terrain are most reliable (Fig. 2). For this reason, these data must slightly (approximately by the height of the crater rim crest above the surrounding terrain) differ from the shifted-image data.

Figure 3 shows two series of data obtained during the flight of two spacecraft to Venus: the earlier Soviet *Venera-15* and *Venera-16* spacecraft (1983–1985) and the later *Magellan* spacecraft (USA, 1992–1995). We discussed the problem of comparing the depth–diameter relationships for craters on various planetary bodies in a collective paper (McKinnon *et al.*, 1997).

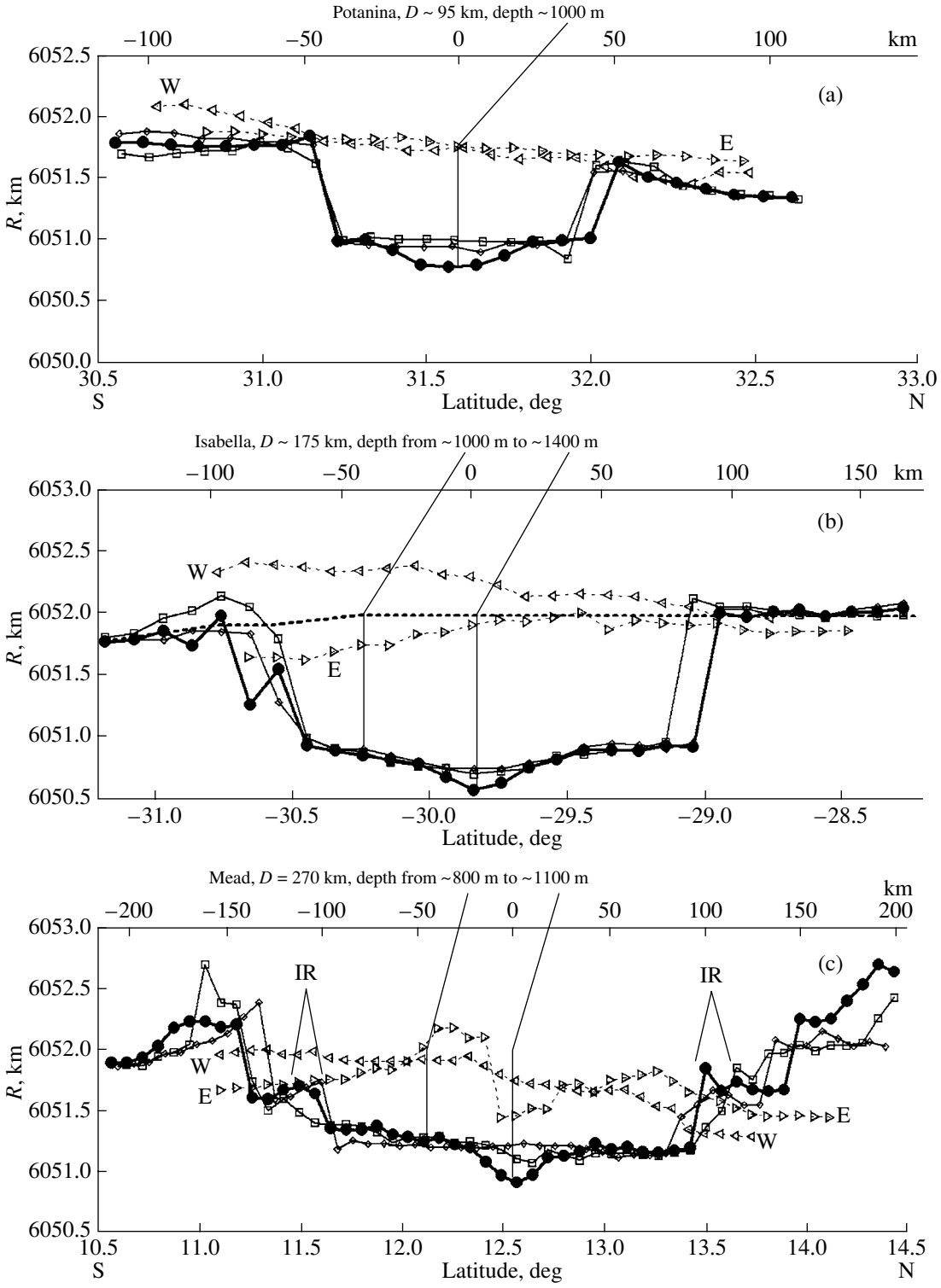

Fig. 2. Altitude profiles along the *Magellan* radio-altimeter tracks (approximately in the south–north direction) crossing the crater near the center (filled circles, diamonds, and squares). The additional tracks passing to the left and to the right (respectively, to the west and to the east) of the crater (leftward and rightward triangles) give an idea of the original surface level. Estimates of the crater depths below the level of the surrounding terrain are shown in the panels. The original data were specially processed by the team of at Massachusetts Institute of Technology when preparing a joint paper (Ivanov and Ford, 1993): (a) the Potanina crater, (b) the Isabella crater, and (c) the Mead crater.

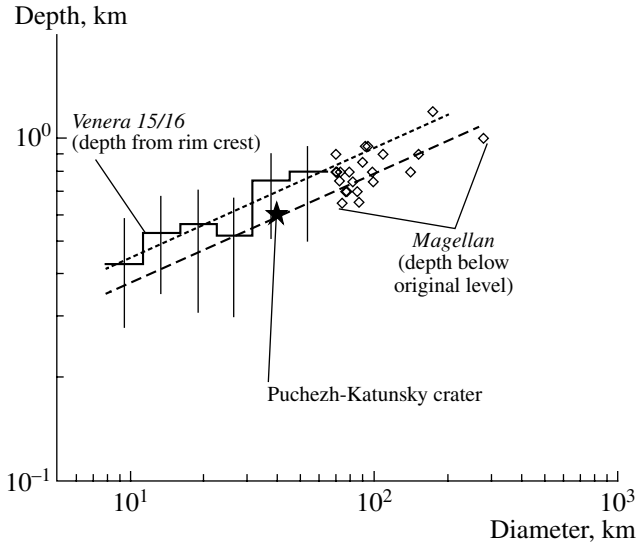

Fig. 3. Depth of Venusian craters versus their rim crest diameter. The estimates obtained by the shifted-image method (Ivanov, 1989) for the depth below the rim crest are given for craters less than 70 km in diameter; the *Magellan* radio-altimetric data are given for craters more than 70 km in diameter. The depth of the terrestrial Puchezh-Katunsky crater is shown for comparison.

The scatter of points for the depths of large Venusian craters shows that each large crater has its own peculiar features. The visible depths (the depths below the surrounding terrain) of craters of the same diameter can differ by 100–200 m. In general, the depth of Venusian craters with diameters from 100 to 300 km is about 1 km. It seems possible that the deviation of the depths from the mean relationship can reflect the influence of differences in the properties of the projectile and the target, which in one way or another affect the final crater depth.

NUMERICAL MODELING OF THE FORMATION OF LARGE TERRESTRIAL CRATERS

We numerically computed a vertical crater-forming impact for two- and three-layer targets that reproduced the sedimentary cover, the terrestrial crust, and the upper mantle or the two-layer terrestrial crust and the upper mantle. Since the resolution of the computational grid (the cell size in the central region) was 200–350 m, a layering thinner than 1–3 km could not be resolved into separate layers. Such a resolution allowed us to specify a spherical projectile with a resolution of about 40 cells for the projectile diameter. This is believed to be enough to reproduce, for example, the volume of melted rocks with an accuracy of about 10% compared to the computations in which the projectile was represented by twice the number of computational cells (Pierazzo *et al.*, 1997). The chosen compromise between the accuracy of representing the projectile and the overall size of the computational grid allowed the computations to be performed on a grid with a constant cell size without increasing it at late computational stages. The formation of a crater was computed up to a physical time of 400–800 s, which, in general, was enough for the final crater shape to be formed. The initial approximation for the projectile diameter was chosen from the scaling laws suggested previously (Schmidt and Housen, 1987). Subsequently, we chose the projectile diameter (and, more rarely, the speed) by trial and error and then varied the model parameters for which no reliable experimental data were available (mainly the AF model parameters). We performed from 10 to 30 computations for each of the craters considered below, which allowed us to estimate the stability of the results to variations in the parameters. These results require a detailed discussion that is beyond the scope of this paper, where the main objective is to demonstrate the approach to comparing numerical models and observational data. Therefore, as a rule, we will present the results of the "best" computations that, in our opinion, are most useful for a further improvement. Below, we discuss computational results for the four largest craters found on the Earth. For the unity of our discussion, for each crater we will give brief information about the target properties and references to special literature containing the geological and geophysical data on each impact structure known to date.

The Popigai meteorite crater was produced by the impact of a stone asteroid (Masaitis and Raikhlin, 1986) about 36 Myr ago (Bottomley *et al.*, 1997) near the northern boundary of the Anabar shield (Rosen *et al.*, 1991; 1994). The Anabar shield is an area of the (strongly modified) ancient continental crust that began to consolidate ~3.7–3.8 Gyr ago (Structure of the Terrestrial Crust of the Anabar Shield, 1986). The complex structure of the northern part of the shield can be roughly represented as a sequence of increasingly dense crustal rocks overlying the crust/mantle interface at a depth of ~40 km.

The visible structure of the target at the impact site includes layers of Archean gneisses covered with an inhomogeneous sedimentary and metasedimentary cover whose thickness seems to have increased from zero in the southeastern part of the future crater to ~1 km near the future northeastern wall of the crater (Masaitis *et al.*, 1975; Masaitis, 1994). A brief history of the discovery of the crater and a description of its geology can also be found in Deutsch *et al.* (2000). The layer of sedimentary rocks at the impact site is assumed to be no more than 400 m in thickness, which is much less than the presumed projectile diameter (D_{pr} ~ 8 km at a speed of 15 km/s). Although the presence of sedimentary rocks is crucial for understanding the conditions at the impact site and the origin of the unique shock-metamorphized rocks, a layer of such a thickness could not affect significantly the overall patter of crater formation as a complex depression. Therefore, in the computations described here, we adopted a two-layer (a granite crust overlying a dunite mantle) or three-

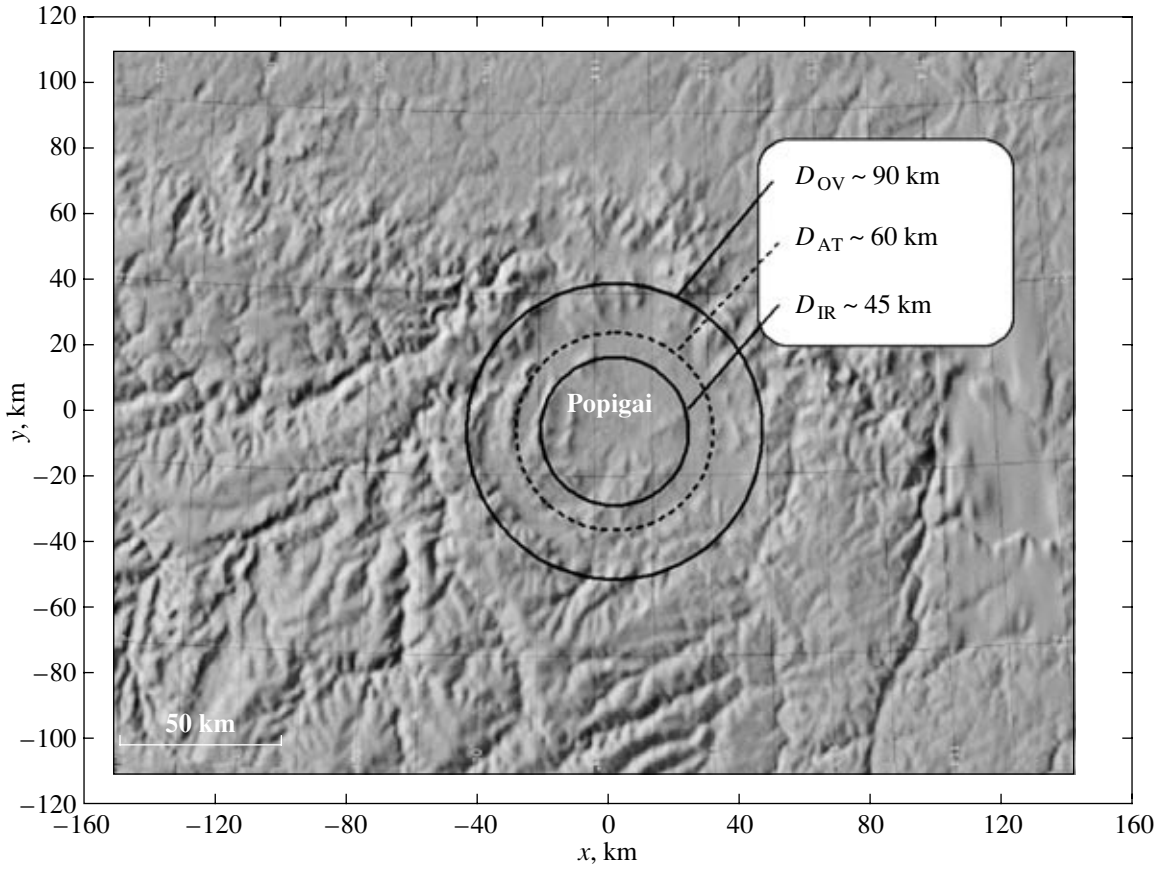

Fig. 4. Shadow map of the relief near the Popigai meteorite crater (constructed using a Web program accessible at http://jules.unavco.org—UNAVCO Boulder Facility and the Jules Map server homepage Web site). The circumferences correspond to the main morphological features of the crater drawn using a geological map and a map of gravity anomalies (Masaitis, 1998; Masaitis *et al.*, 1998). D_{OV} is the outer visible diameter (slightly smaller than the initial diameter at the wall crest), D_{AT} is the diameter of the axis of the annular trough, and D_{IR} is the inner rim crest that roughly corresponds to the ring uplift.

layer (an upper crust, a lower crust, and a mantle) target structure.

At present, Popigai is a round depression in which the following is embedded:

—a central depression bounded by a ring uplift of crystalline basement rocks. The ring uplift (inner ring) has a diameter of D_{IR} ~ 45 km (Fig. 4);

—an annular trough with an axis diameter of D_{AT} ~ 60 km and an outer diameter of 72–75 km;

—an outer visible boundary of the crater depression whose diameter can be estimated to be D_{OV} ~ 90 km.

In addition, a partly preserved cover of ejecta in the form of allogenic breccias distributed within and outside the ring with diameter D_{OV} belongs to the structure. The rim crest diameter immediately after its formation is estimated to be 100 km (Masaitis *et al.*, 2003).

Geophysical data allow the depth of burial of the crystalline rocks to be estimated at the center of the crater, 2–2.5 km (Masaitis *et al.*, 1998). Allogenic breccias mixed on various scales with the impact melt overlie the crystalline rocks (the authigenic breccia of the central uplift) almost up to the visible surface in the central depression. Breccias rich in the solidified melt cover an area of ~5000 km^2, representing a series of rocks from tagamites (a clast-poor melt) to suevites (a clastic material with a large content of solidified melt fragments). An extensive program of drilling boreholes with a depth as large as 1.5 km performed with the goal of exploring the deposits of impact diamonds (Masaitis *et al.*, 1998) allowed the overall volume of the melt (minus the clasts) preserved in the crater to be estimated, about 1750 km^3 (Masaitis *et al.*, 1980). This value was repeatedly used to calibrate the theoretical relationships between the impact melt volume and the crater diameter and to test the similarity laws (Grieve and Cintala, 1992; 1997; Pierazzo *et al.*, 1997).

We chose the parameters of the computational model for the Popigai crater to obtain a model crater with the observed morphology and a volume of the impact melt close to the observed one. Varying the parameters of the computational schemes yielded acceptable (at a computational cell size of ~200 m) agreement between the model and the observations for the vertical impact of a spherical body with a density of

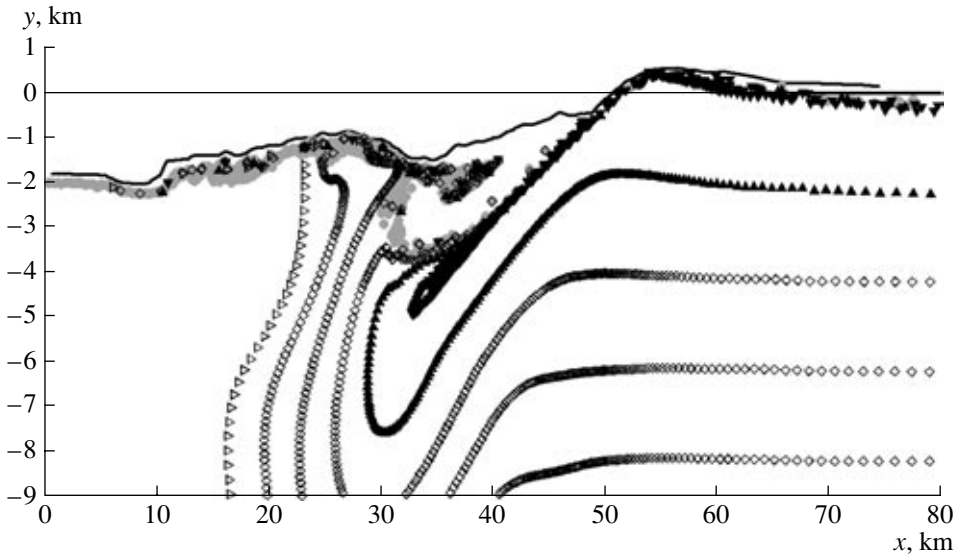

Fig. 5. Profile through the model Popigai crater greatly exaggerated vertically. The symbols correspond to the initially horizontal target layers located at different depths. In the zone of collapse of the crater edge, the original surface subsides to a depth as large as 5 km at a distance of about 33 km from the crater center. The shade of gray indicates the final positions of the massless tracers from the melting zone (a shock pressure ≥50 GPa).

2630 kg/m^3 (the granite equation of state) and a diameter of ~8 km at an assumed impact velocity of 15 km/s. The impact energy was 8×10^{22} J, and the total volume of the impact melt (for dry granite) was ~2600 km^3. The grid resolution is certainly too low to accurately describe the motion of the melt as the crater grows. Rough volume estimations for the melt remaining in the crater yield the following values:

~13% within 20 km of the center,

~30% within 30 km of the center, and

~85% within 40 km of the center.

Given that the melt transport can differ greatly from our computed case for an oblique impact on a wet target under typical conditions of the surrounding atmosphere (i.e., the factors that are disregarded in our computations of a vertical impact on a dry target), the volume of 2000–2200 km^3 of the melt remaining in the central part of the crater is close to the observational estimate of 1750 km^3. The typical thickness estimate for the melt sheet at the crater floor (at a density equal to the initial granite density) is

~150 m within 20 km of the center,

~200 m in the ring with radii from 20 to 30 km, and

~250 m in the ring with radii from 30 to 40 km.

Interestingly, for a purely ballistic motion of the material in the model (there is neither air drag nor gas acceleration by water vapor), the bulk of the melt accumulates on the periphery of the crater depression. In the actual crater, the melt lies in the form of separate bodies immersed in a layer of allogenic breccias.

Figure 5 shows the radial surface profile obtained in one of our computations with the final positions of the tracers from the impact melt zone plotted on it. We see that much of the melt (more precisely, its tracers) is buried in the annular trough at depths as large as 4 km. To clarify this transport of the melt, let us briefly describe the overall pattern of crater formation in the suggested model (Fig. 6).

Figure 6 shows six snapshots in the crater formation process. The crater cavity reaches its maximum depth (~18 km) in about 20 s and begins to collapse immediately after. The collapse of the crater rim leads to an uplift of the crater floor above the original surface level (a maximum "shooting" of ~6 km) about 90 s after the maximum depth is reached (and 115 s after the impact). At this time, the cavity floor is curved upward. Thus, the crater floor covered with a melt sheet becomes the surface of a slowly collapsing hill; in this case, downward flows of hot melt in a mixture with rock debris are possible. By 200 s, the collapse of the hill generates an annular wave of material that spreads over the crater floor. This surface flow of material leads to the burial of part of the melt beneath the floor of the annular peripheral depression, as shown in Fig. 5. First, a high temperature of the material and, second, a low strength of the fragmented material created through lithostatic pressure (which is low in the upper layers) facilitate the flows on the surface of the collapsing hill. Since, as a more detailed analysis of the figures shows, the 200-m resolution is on the verge of the computational grid resolution, the results obtained should be recognized as preliminary and requiring a special modeling with the resolution near the surface of the forming crater increased several-fold.

In our model, the ring uplift at the crater floor morphologically arises from the collapse of the hill. How-

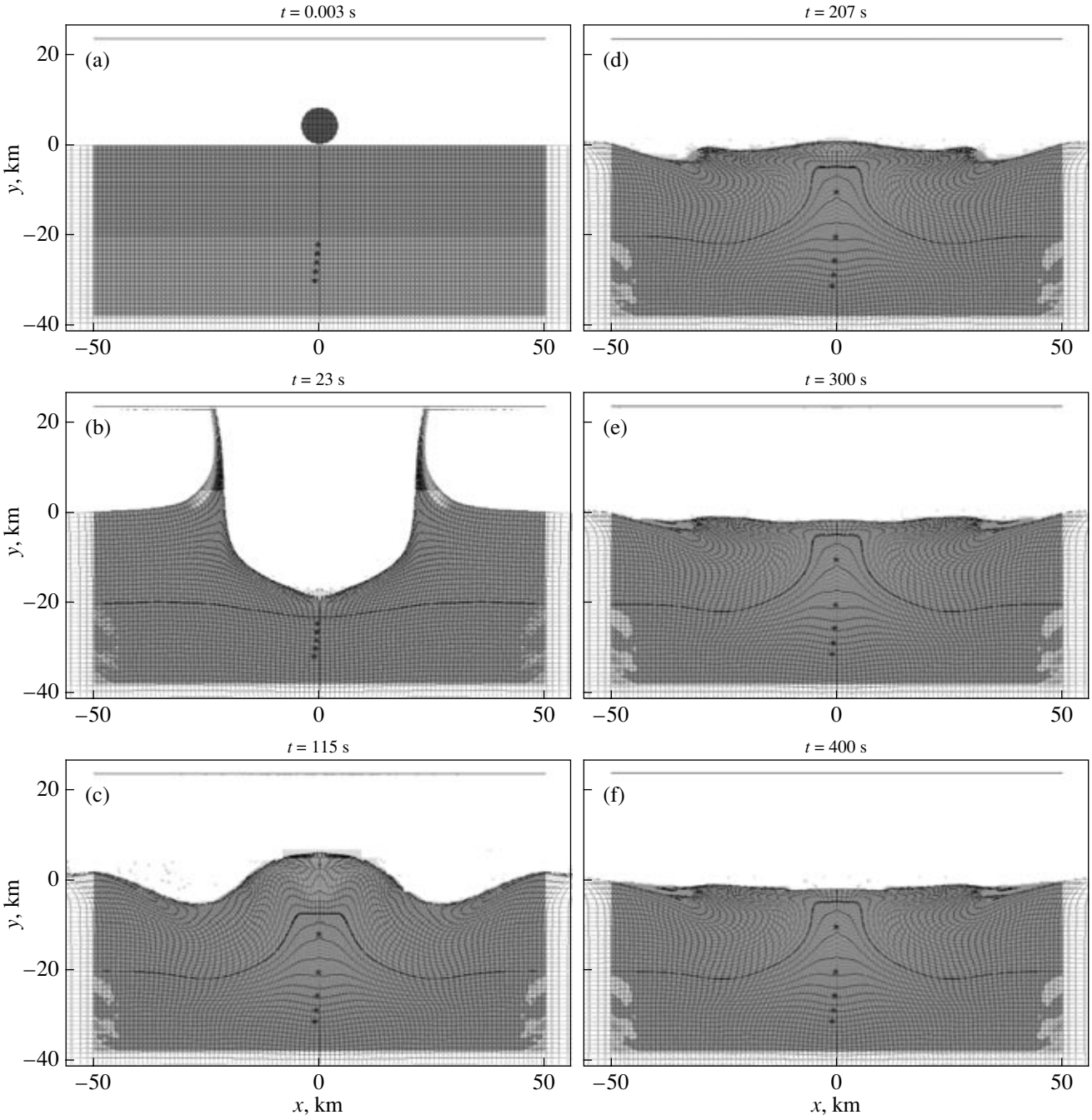

Fig. 6. Sequence of events during the formation of the model Popigai crater: (a) the initial positions of a spherical projectile and a layered target; (b) the 23th second: the transient cavity of the crater reaches its maximum depth of about 19 km; (c) the 115th second: the collapse of the transient cavity (the uplift of rocks in the center through the rim collapse) gives rise to a transient hill up to 5 km in height, the deep rocks under the crater rise above the level of their original burial; (d) the 200th second: the transient hill spreads in the field of gravity, while the deep rocks stop due to the restoration of normal internal friction, the speed of the near-surface spread reaches 200 m/s; (e) the 300th second (5 min after the impact): the motion is close to a stop; (f) 400 second after the impact: the crater assumes a stable final shape.

ever, it should be noted that the collapse of the transient crater cavity itself, which gives rise to the hill, results from a large structural uplift of the floor of the growing crater that accompanies the uplift of the crustal layers initially buried at a depth of ~18–20 km to the surface. According to the geophysical model for the northern edge of the Anabar shield (Structure of the Terrestrial Crust of the Anabar Shield, 1986, Fig. 48), the denser rocks of the lower crustal layer with a density of ~3 g/cm^3 lie below this level; therefore, it is unlikely that the uplift beneath the crater center can easily be noticed in the field of the gravity anomaly measured

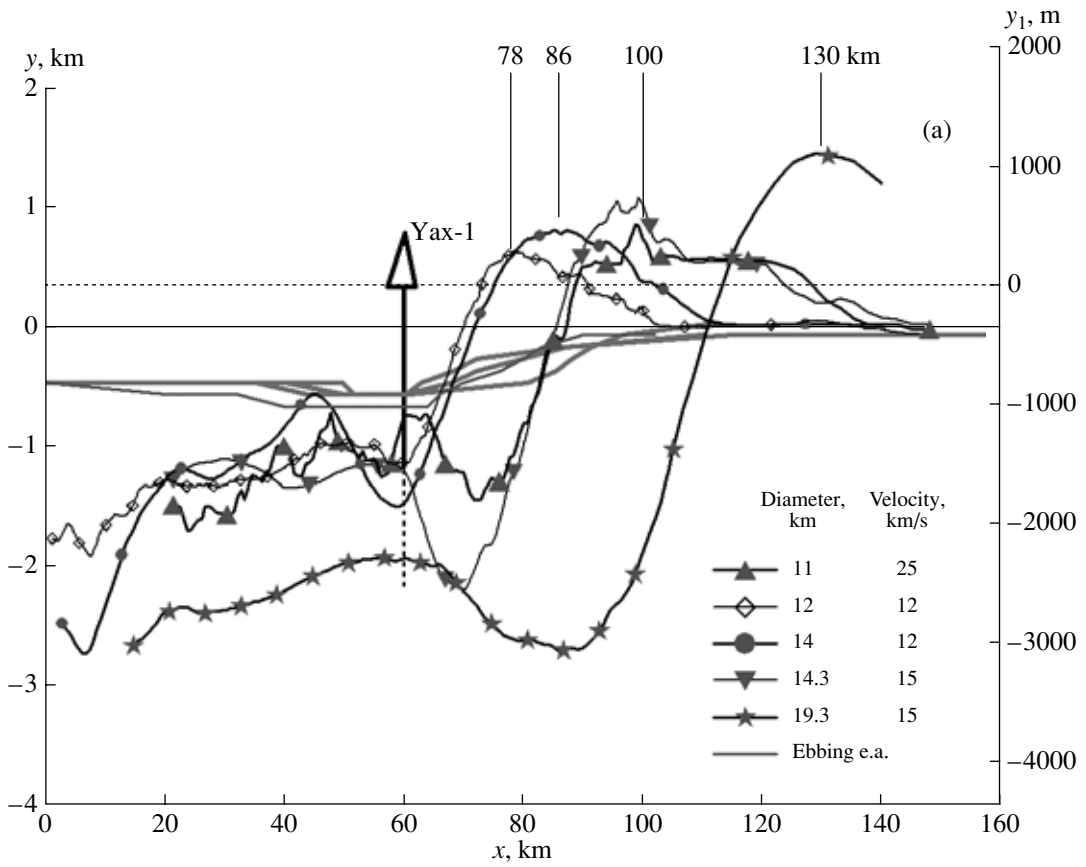
y, km
y1, m
78
86
100
130 km
(a)
Yax-1
Diameter, km
Velocity, km/s
11 25
12 12
14 12
14.3 15
19.3 15
Ebbing e.a.
x, km

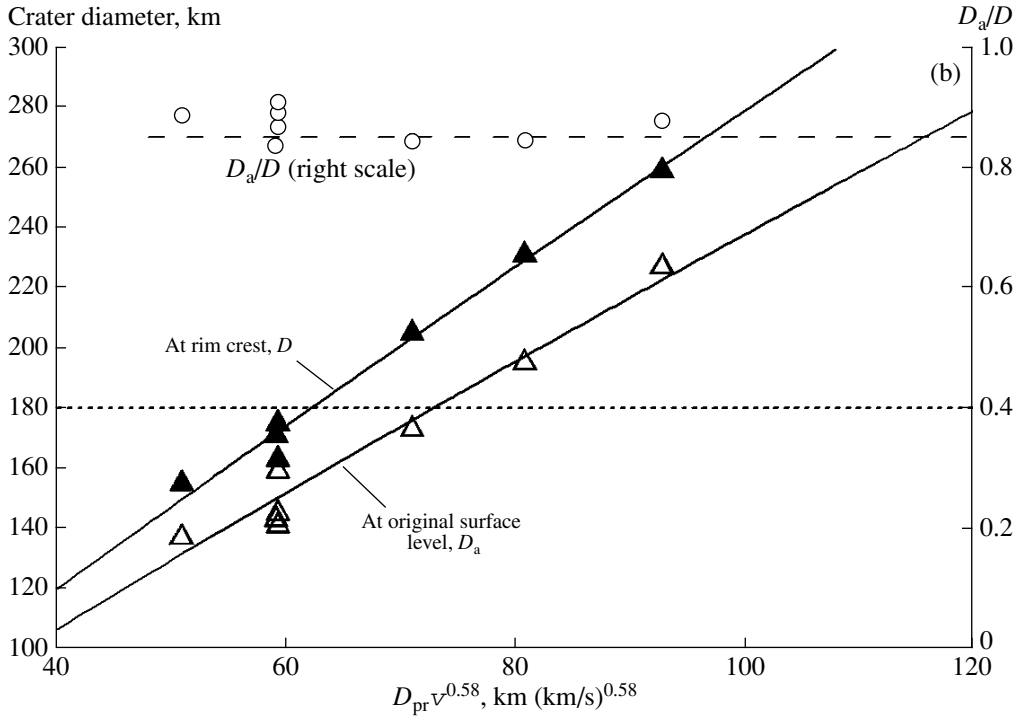
Crater diameter, km
Da/D
(b)
Da/D (right scale)
At rim crest, D
At original surface level, Da
Dpr v^0.58, km (km/s)^0.58

under the crater. Besides, the uplift of rocks from large depths is accompanied by their fracturing and decompaction, which the lithostatic pressure is probable unable to suppress at depths of less than ~5 km (a typical estimate of the closure of microfracturing in rocks).

The minimum crater depth of ~2 km obtained in our computations most likely corresponds to the depth of the cover of authigenic breccias at the center of the structure, since the computations were performed without including the atmospheric effect; the deceleration of ejecta in the atmosphere produces a flow of material returned to the crater through the settling from a gas–dust cloud.

Thus, in our numerical computations, we obtained a model crater that is qualitatively (and, in many parameters, quantitatively) similar to the Popigai meteorite crater.

The **Chicxulub meteorite crater** was produced by the impact of an asteroid about 65 Myr ago. The global spread of traces of the projectile material associated with this impact event (iridium anomaly) and a fine fraction of ejecta (shocked quartz) and the concurrence of the formation with mass extinction at the Cretateous-Tertiary (K/T) boundary formed the basis for the hypothesis about the very appearance of the K/T boundary as the result of a giant impact (Alvarez *et al.*, 1980). Interestingly, first, global traces of the impact event were found and the impact scale was estimated, and only several years later was the Chicxulub meteorite crater discovered on the north coast of the Yucatan Peninsula (Mexico) (Hildebrand *et al.*, 1991).

Morphologically, the Chicxulub impact structure is a crater with a central ring uplift with an apparent outer diameter of the crater depression of ~180 km, approximately twice as large as that for Popigai. Consequently, the asteroid that produced Chicxulub during its impact was also twice as large in diameter as that for Popigai. Typical estimates lie within the range from 10 to 14 km (Hildebrand *et al.*, 1991; Ivanov *et al.*, 1996; Swisher *et al.*, 1992).

The currently observed complex crater structure was formed through the collapse of a transient cavity from 90 to 120 km in diameter (Ivanov *et al.*, 1996; Morgan *et al.*, 2000; Pierazzo *et al.*, 1998; Pierazzo and Melosh, 1999).

Seismic sounding, geophysical modeling, and drilling have revealed general structural features of the crater that is now buried beneath a layer of younger sediments ~1 km in thickness. To all appearances, many structural features of the crater that were destroyed in other structures have been preserved under the sediments. For example, a solid cover of ejecta was partly preserved south of the crater (Pope *et al.*, 1994, 1997).

According to geological and geophysical data (Morgan *et al.*, 1997), we simplified the target structure for our numerical computations to three layers: a 3-km-thick upper sedimentary layer (the equation of state for calcite), a crystalline basement (the equation of state for granite), and a mantle into which the basement transforms at a depth of 33 km (the equation of state for dunite). As above, the interaction between the atmosphere and the ejecta was not computed—the flight of the ejecta and the cloud expansion took place in a vacuum. Previously, we published preliminary results of our numerical modeling of the crater in a two-layer (crust/mantle) target (Stöffler, 2004).

The model parameters were initially chosen (Ivanov, 2003a) by widely varying the projectile parameters. Figure 7a shows the model crater profiles for the vertical impact energy of a spherical projectile varied from 2.2×10^{22} to 7.4×10^{22} J (the projectile diameter varied from 14 to 19 km, the impact velocity varied from 12 to 15 km/s).

Since the mechanical action at a high-velocity impact is determined by the specific combination of the projectile diameter and the impact velocity (for the same ratio of the projectile and target densities), we chose the so-called efficiency parameter (Dines and Walsh, 1973)

$$L = D_{\mathrm{pr}} v^{0.58}, \quad (5)$$

where D_{pr} is the projectile diameter, and v is the impact velocity. Figure 7b shows how the crater diameter increases with efficiency parameter. As the crater diameter increases from ~150 to 250 km, the ratio of the visible (at the original surface level) diameter of the crater to its rim crest diameter remains almost constant (Fig. 7b). The depth of the final crater also increases very slowly, roughly in the same way as for Venusian craters (cf. Figs. 3 and 7a).

The overall pattern of motion of the material is roughly similar to that shown in Fig. 6 for the Popigai crater: the growth of a deep transient cavity, its collapse, the uplift of the crater floor, its evolution into a

Fig. 7. Model crater diameter versus asteroid size and speed. (a) The model crater profiles in several model runs performed when choosing parameters to reproduce the Chicxulub crater. The rim crest radii vary between 78 and 130 km (accordingly, the crater diameter varies between ~160 and 260 km). The position of the Yaxopol-1 borehole is also shown. The left height scale is given relative to the target surface at the impact time. On the right height scale, the zero level was shifted by the thickness of the sedimentary layer under which the crater is buried at present. The diameter and speed of a spherical projectile for each computation are shown in the inset. The gray lines without symbols indicate the currently observed crater profiles (minus the younger sediments) drawn in various azimuthal directions (Ebbing *et al.*, 2001). (b) Crater rim crest diameter (filled triangles) and at the original surface level (open triangles) versus impact efficiency parameter (Eq. (5)). The circles (right scale) indicate the ratio of the diameters at the original surface level and at the wall crest, which is, on average, 0.82. The horizontal dotted line indicates the commonly mentioned estimate of the visible crater diameter, 180 km.

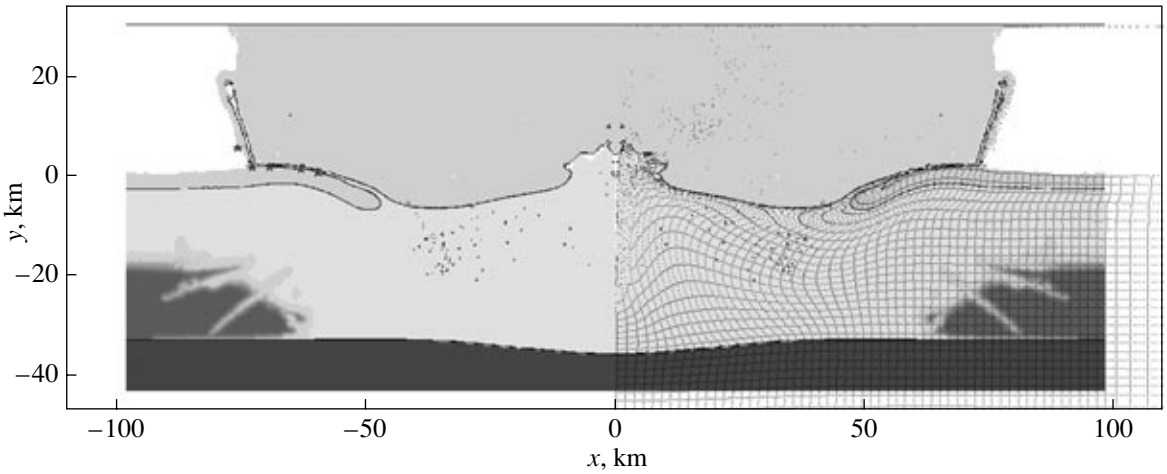

Fig. 8. Cross section of the growing Chicxulub crater 128 s after the impact. The mantle is indicated by the dark shade at the bottom. The expanding gaseous products of the thermal decomposition of the upper sedimentary layer (limestone) are indicated by the shade of gray in the upper part. Within the crust, the rocks in which the strength limit was not exceeded are indicated by darker zones. The sideways expansion of the gaseous products is bounded by the plume of ejecta.

hill raised above the surface, and the collapse of the hill to produce an indistinct (in our computations) uplift. However, in the case of Chicxulub, the proximity of the mantle surface creating a contrasting density boundary prevents the uplift of the crustal rock layers immediately beneath the crater center—the transient cavity collapses with part of the melt being captured into a vertical stock on the symmetry axis. This leads to a distortion of the initially flat layers on the symmetry axis at a depth of less than 20 km (Fig. 8).

An additional difference is the presence of a large amount of vapors expanding in the upper half-space—a result of the "early" vaporization at a temperature of ~1500 K imitating the long discussed possibility of thermal decomposition of calcite and anhydrite behind a fairly strong shock wave included in the equation of state for limestone (for a discussion, see Gupta *et al.*, 1999; Ivanov *et al.*, 1996; 2004; Langenhorst *et al.*, 2003; Pierazzo *et al.*, 1998). According to the fairly popular model by Pope *et al.* (1994, 1997), the enormous amount of sulfur dioxide thrown into the stratosphere during the impact and the anhydrite decomposition in the sedimentary cover could be responsible for the biota mass extinction as a result of the formation of the Chicxulub crater.

The model for the internal structure of the crater (Christeson *et al.*, 2001; Ebbing *et al.*, 2001; Morgan *et al.*, 1997; Pilkington and Hildebrand, 2000) constructed from seismic survey data and geophysical field anomalies allows a direct comparison to be made between the model and the observations. Such a comparison makes it possible to choose the best (of those tested to date) set of model parameters ensuring that the model is plausible when compared with the observations.

The mutual arrangement and relative sizes of the asteroid at the impact time, the future impact melt zone, and the future zone of ejecta are schematically shown in Fig. 9a. We clearly see that part of the melt zone is located in the sedimentary layer—this is the zone where the melting and thermal decomposition of calcite and anhydrite are possible. In 2002, the Yaxcopoil-1 (Yax-1) borehole ordered by the International Continental Drilling Project (ICDP) was drilled at 60 km from the Chicxulub center. The computations partly described here were performed to analyze the drilling results. This analysis was published by Stöffler (2004). Figure 9a shows the initial positions and trajectories of the particles that deposited at distances between 55 and 65 km from the crater center (plus/minus 5 km from the nominal distance of the Yax-1 borehole). Also shown here is the subsidence of the layer of sediments and its overturning near the boundary of the zone of ejecta. In this case that is closest (of those accumulated in this paper) to the geophysical data on the crater structure (Fig. 9b), the layer of sediments during the collapse of the transient cavity subsides to a depth of ~10 km at a distance of ~40 km from the crater center. Geophysicists draw approximately the same picture based on seismic sounding data and analysis of the gravity and magnetic anomalies beneath the crater. Figure 9b shows the central column of melt squeezed between the walls of the collapsing cavity (in reality, this must be a zone of rock debris mixed with melt). However, the central basin of impact melt extending to a distance of ~40 km from the crater center constitutes more than half of the impact melt of the crystalline basement material in the model. Unfortunately, the model presented here does not reproduce the faults and upthrusts of rocks as the crater collapses. These results should be tested in the future using three-dimensional model com-

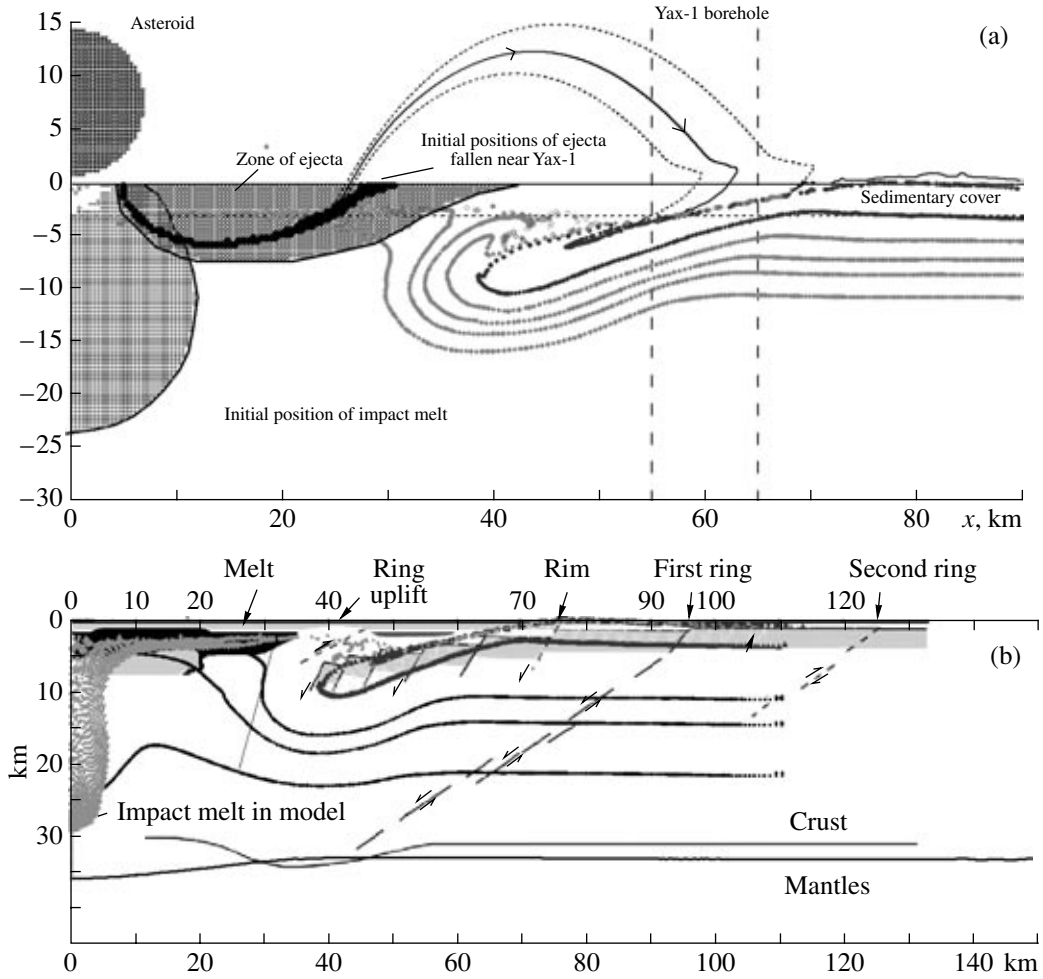

Fig. 9. Cross section of the model Chicxulub crater. (a) the arrangement of the impact melt zone and the zone of ejecta during the crater formation. The spherical projectile producing the crater is shown for comparison. The deformation of the initially horizontal target layers is shown below the surface level. The trajectories of several tracers that deposited near the Yaxopol-1 drilled borehole in a ring with a radius of 60 ± 5 km at the final positions are indicated by the vertical dotted lines. The shade of gray within the zone of ejecta highlights all of the tracers with the final positions after their separation within this ring. (b) The cross section of the model crater superimposed on the crater structure scheme constructed from geophysical data, including seismic sounding at several profiles (Morgan *et al.*, 1997; 2000). The melt zone in the model crater consists of the melt layer at the crater floor and the stock of melted rocks gripped near the symmetry axis during the collapse of the transient cavity bounded by the crust–mantle boundary. The deformation of several initially horizontal crustal layers (the lines of almost merging dark symbols) is shown. The solid lines at depths below 30 km indicate the crust–mantle boundary in the computation and on the geophysical profiles.

putations in which there are no conditions for the anomalous motion of matter near the symmetry axis.

No diamonds have been found in the rocks transformed during the impact that produced Chicxulub so far. However, even in this case, the formation of a giant (by terrestrial standards) crater gave rise to a mineral deposit. The Chicxulub crater was formed on the surface of a carbonate platform that terminates fairly steeply at distances of ~300 km from the crater center (the platform edge is known as the Campeche terrace). The seismic action of the impact is believed to have led to the mass underwater collapse of the terrace. The dolomitization of limestones on the surface of the underwater landslide produced an impervious crust under which an oil–gas field was formed (Bralower *et al.*, 1998; Grajales-Nishimura *et al.*, 2000; Ricoy, 2003). At present, it gives about 2/3 of the entire oil production in Mexico, bringing ~16 billion dollars per year to the country on the territory of which the Chicxulub crater was formed (Donofrio, 1998).

To verify the possibility of catastrophic collapse of the underwater slope at such a distance from the impact site (the arrangement is schematically shown in Fig. 10), we performed computations using the same SALEB program on a coarser grid (with a cell size of 0.5 and 1 km). This allowed us to reproduce the pattern of vibrations at a distance of 300 km within the first 100 seconds after the impact (Fig. 11). At later times, the pattern of vibrations is still reliable, but the elastic waves reflected from the boundary of the computa-

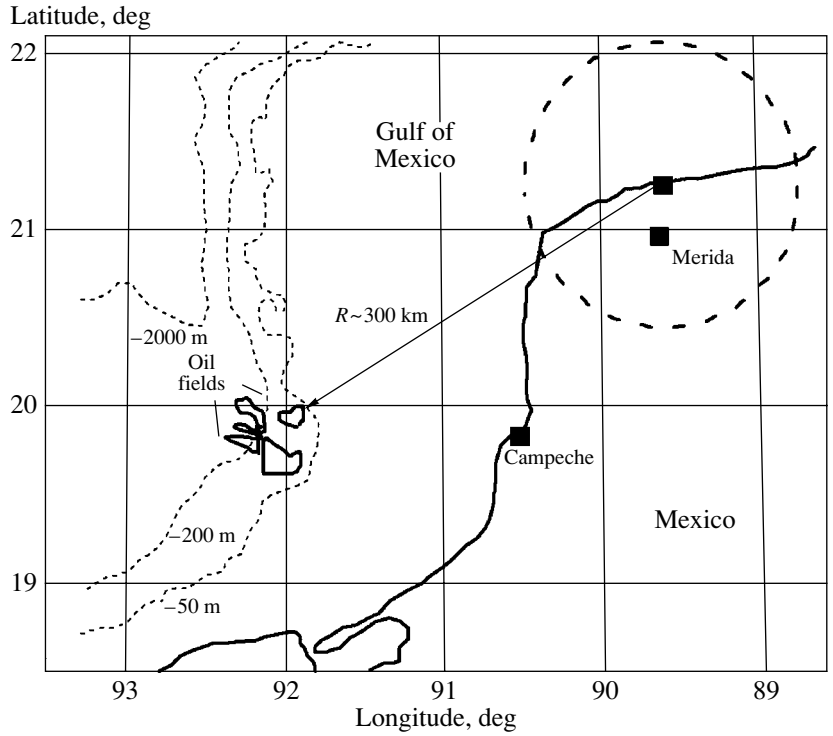

Fig. 10. Map of an area of the Yucatan peninsula coast shows the relative positions of the Chicxulub crater (dotted circle) and the oil fields near the Campeche underwater terrace bounding the carbonate platform of the peninsula. Several isobaths give an idea of the transition of the continental shelf to the bottom of the Gulf of Mexico. The submarine landslide in which the oil field was formed is believed to have been initiated by a seismic wave from the crater-forming impact (Bralower *et al.*, 1998).

tional region already begin to have an effect. We see that the vibration velocity in a seismic wave at a distance of 300 km is ~10 m/s at displacements of ~70–80 m. Such vibrations seem to be strong enough to destabilize the underwater slope, although this question deserves a special analysis. Here, we restrict ourselves to a simple estimation. Based on the standard formulas for comparing the explosion and earthquake seismic energies (see, e.g., Dahlman and Israelson, 1977), we can roughly (the amplitudes are too large) compare the vibrations shown in Fig. 11 to earthquake vibrations with a magnitude M_W from 10 to 11. Extrapolating the available data (for earthquakes with maximum recorded magnitudes $M_W \sim <9.5$) allows the distances at which the stability of the watered soil can be lost as ~500 km (Dutta *et al.*, 2003; Papadopoulos and Plessa, 2000).

To summarize the attempts to model the formation of the Chicxulub crater, it should be noted that the simplified three-layer model for the target structure cannot reproduce all of the complex phenomena related to the presence of partially watered evaporites. The possible thermal decomposition of limestone and anhydrite as well as the water evaporation of shallow lakes changes significantly the pattern of motion of the early ejecta, especially in the case of an oblique impact (Stöffler, 2004). However, the relatively low cost of two-dimensional computations (compared to three-dimensional ones) makes the simple axisymmetric problems attractive for a parametric analysis of existing models and their improvement. In the case of a buried impact crater, which Chicxulub is, numerical computations that ensure the conservation of mass, momentum, and energy in describing the motion of material will undoubtedly help construct more realistic solutions of inverse geophysical problems.

The **Vredefort impact structure** is located in South Africa (S 27°0′, E 27°30′) and is 2023 ± 4 Myr old. The structure has been studied in detail and described in the literature. Recent publications of new observations and geophysical field modeling for the Vredefort structure (Lana *et al.*, 2003a; 2003b; 2004; Moser *et al.*, 2001; Wieland *et al.*, 2003; Wieland and Reimold, 2003) supplement the general reviews (Grieve and Therriault, 2000; Reimold and Gibson, 1996).

For a brief description of the geological situation in which the crater was formed, the following should be noted. In general, the Vredefort impact structure was formed within a large ancient block of the Archean lithosphere called the Kaapvaal craton. Apart from scientific interest, intensive geophysical studies were associated with the proximity of the economically important Kimberley diamond fields. Here, studies of the propagation of seismic waves allowed the crust–mantle boundary to be identified at a depth from 38 to 40 km (Doucoure *et al.*, 1996; Nguuri *et al.*, 2001). The

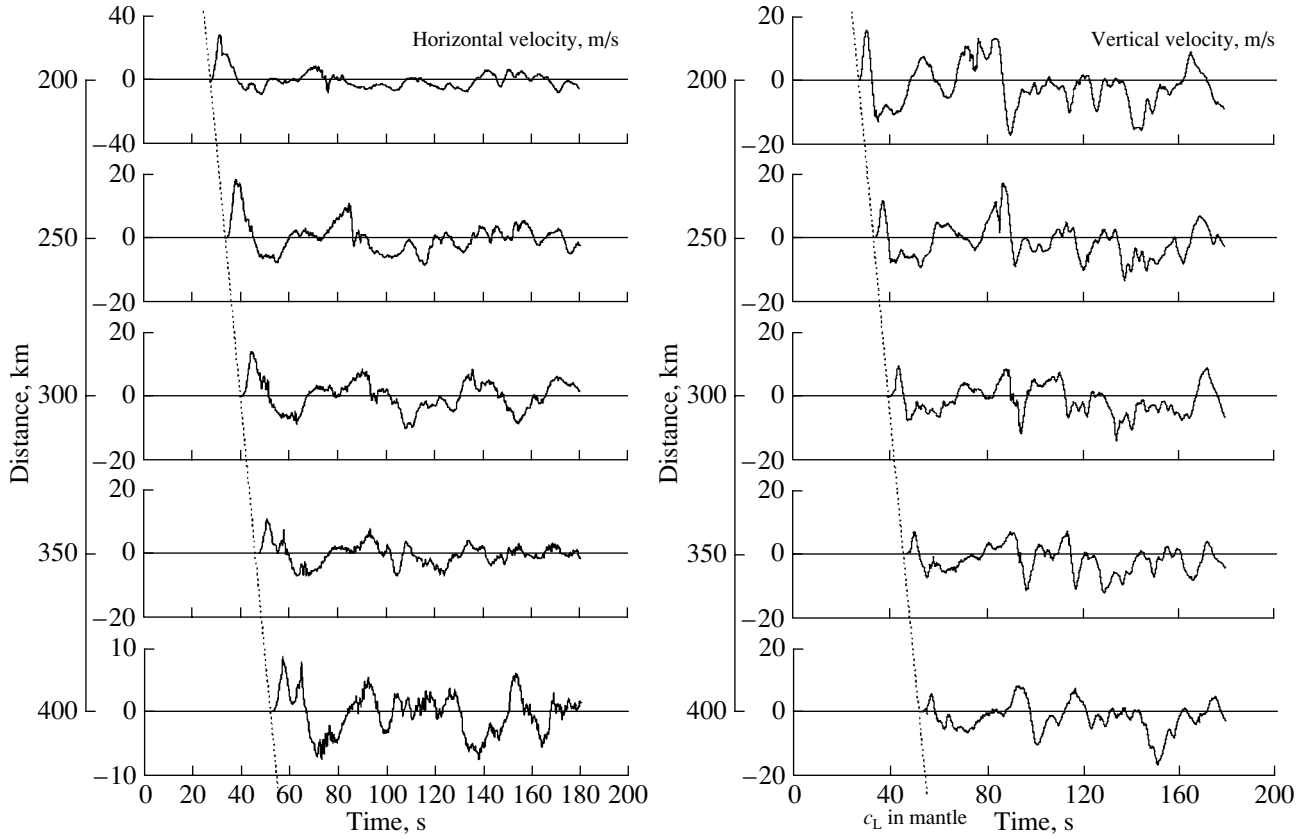

Fig. 11. Model seismograms obtained when computing the impact formation of the Chicxulub crater in the sedimentary layer at distances from 200 to 400 km. At a distance of 300 km (Fig. 10), the vertical and horizontal vibration velocities reach 10 m/s or more. The seismic wave arrival is determined by the longitudinal wave velocity in the mantle, $c_L \sim 8.3$ km/s (the hodograph of this wave is indicated by the inclined dotted line). The rock displacements reach 70–100 m in a wave train with a period of 10–20 s. The accelerations reach 1–1.5 g.

upper mantle beneath the Kaapvaal craton is characterized by reduced seismic velocities (James *et al.*, 2001). According to these studies, about 40 Myr before the formation of the Vredefort crater, the intrusion of igneous rocks of the Bushveld complex (~2060 Myr old) occurred. This could locally produce regions of a high thermal gradient, up to 40 K/km near the surface (Gibson and Jones, 2002). In general, however, the crater formation region had a thermal gradient from 15 to 20 K/km near the surface and a temperature of ~900 K at the crust–mantle boundary (at a depth of ~40 km) (Gibson and Jones, 2002).

The geological history of the Kaapvaal craton includes periods of predominance of tensile stresses during which depressions (basins) filled with sedimentary material were formed (de Wit *et al.*, 1992). When the sediments reached a significant thickness (15–20 km), they were subjected to metamorphism, transforming into mechanically strong rocks (metasediments). The Vredefort crater was formed in such a basin (the Witwatersrand basin), which was produced in several stages 2.97–2.1 Gyr ago (see the review by Gibson and Jones (2002) and references therein). Subsequently, the crater region was subjected to significant erosion (to a depth of 5–10 km). Erosion destroyed all of the near-surface features typical of impact craters (the crater rim, the zone of ejecta, etc.), but, at the same time, exposed the deep structure of the giant meteorite crater. In particular, this is why it is so important to construct a model for the formation of the Vredefort crater; such a model, on the one hand, can give an insight into the structure of the crater before erosion and, on the other hand, allows the principles of numerical modeling to be tested.

The most characteristic feature of the preserved structure is the presence of a granitoid core at its center surrounded by younger rocks, the so-called Vredefort dome (Fig. 12). Geological and geophysical studies have shown that the granitoid rocks were lifted at least by 10–15 km and are midcrust rocks (Henkel and Reimold, 1996; Lana *et al.*, 2003b; 2004; Reimold and Gibson, 1996; Stevens *et al.*, 1999).

Previously, several attempts have been made to model the formation of the Vredefort crater (Turtle and Pierazzo, 1998; Turtle *et al.*, 2003). In these papers, the numerically modeling of the impact was used to compute the initial impact stage, the shock propagation. The excavation stage of the transient cavity was

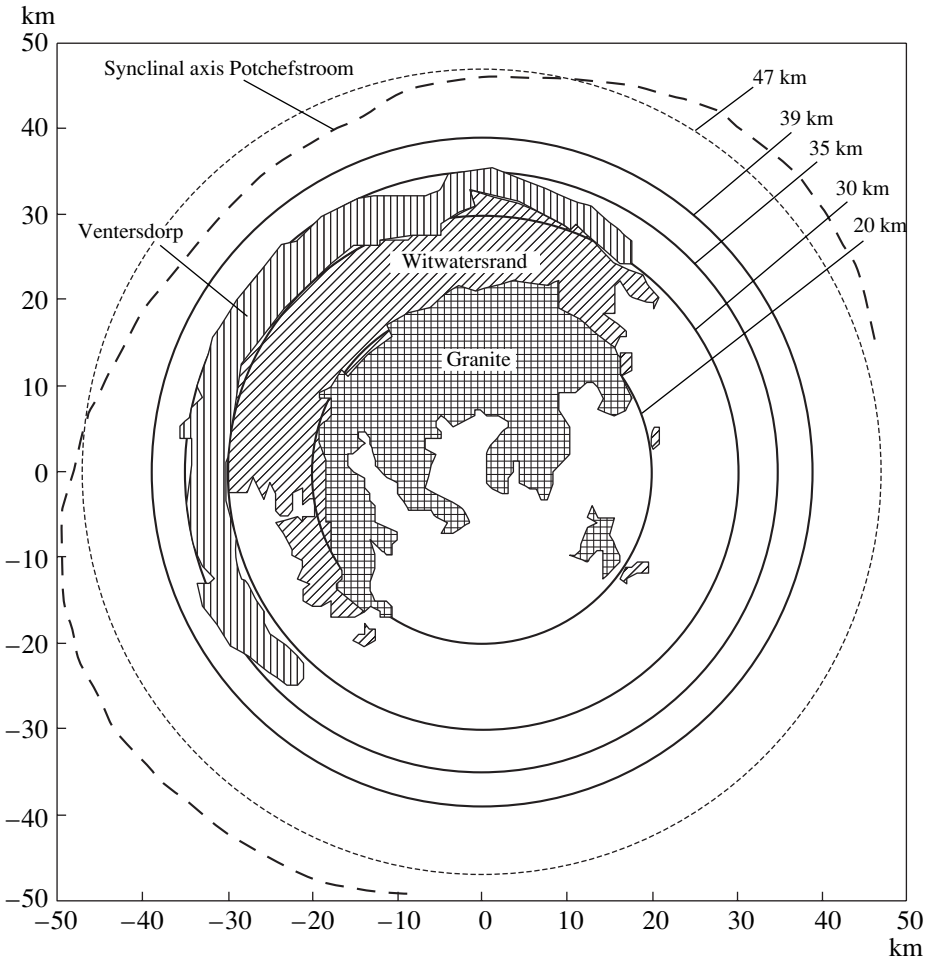

Fig. 12. Schematic geological map of the Vredefort dome from published data (Lana *et al.*, 2003a; Reimold and Gibson, 1996; Therriault *et al.*, 1997). The circumferences that roughly correspond to the zonality of crustal rocks at the present erosion surface are shown.

described analytically using the so-called Z-model. The collapse of the transient crater was computed by a quasi-static finite-element method. Quite plausible estimates of the initial sizes of the crater with a diameter of ~180 km were obtained. In this paper, we present an end-to-end computation using a single code, from the impact time to the formation of the final crater, with a spatial resolution comparable to that in the model of the early stage (Turtle and Pierazzo, 1998).

For the numerical modeling, the target was represented as three layers: a layer of metamorphized sediments, a layer of granitoids, and an underlying mantle. We used the following triples of target materials (from the top downward): quartzite/granite/dunite, granite/basalt/dunite, and granite/basalt/dunite. At the available accuracy in the model used, we found no strong effects when using various model equations of state to describe the crustal material; in general, the mechanical properties of these rocks are similar. For our study, after a review of published sources, we chose a thickness of 14 km for the layer of metamorphized sediments and a depth of 45 km for the crust–mantle boundary as the first approximation. Since the erosion depth is uncertain, these values can vary over a wide range.

Test computations allowed us to choose a projectile (with the model granite density) diameter of about 14 km at the presumed impact velocity of 15 km/s. Figure 13 shows the profile of the model crater for the computation in which the best agreement with geological data at the level of the erosion cut was obtained. It should be noted that in this computation, the shape of the crater might not have been achieved by the time of 400 s when the computation was stopped (in Fig. 13, we see the central uplift instead of the central depression characteristic of Venusian craters). In other computations, the crater was similar to the Popigai and Chicxulub model craters.

The diameter of the model crater shown in Fig. 13 is 172 km at the rim crest and 130 km at the original surface level. The computed volume of the impact melt was ~13000 km^3, with approximately equal melt fractions of the layer of metamorphized sediments and the granitoid basement. At the final computational time, ~25, 50, and 90% of the melt were closer than 20, 40, and 80 km from the impact site, respectively. The char-

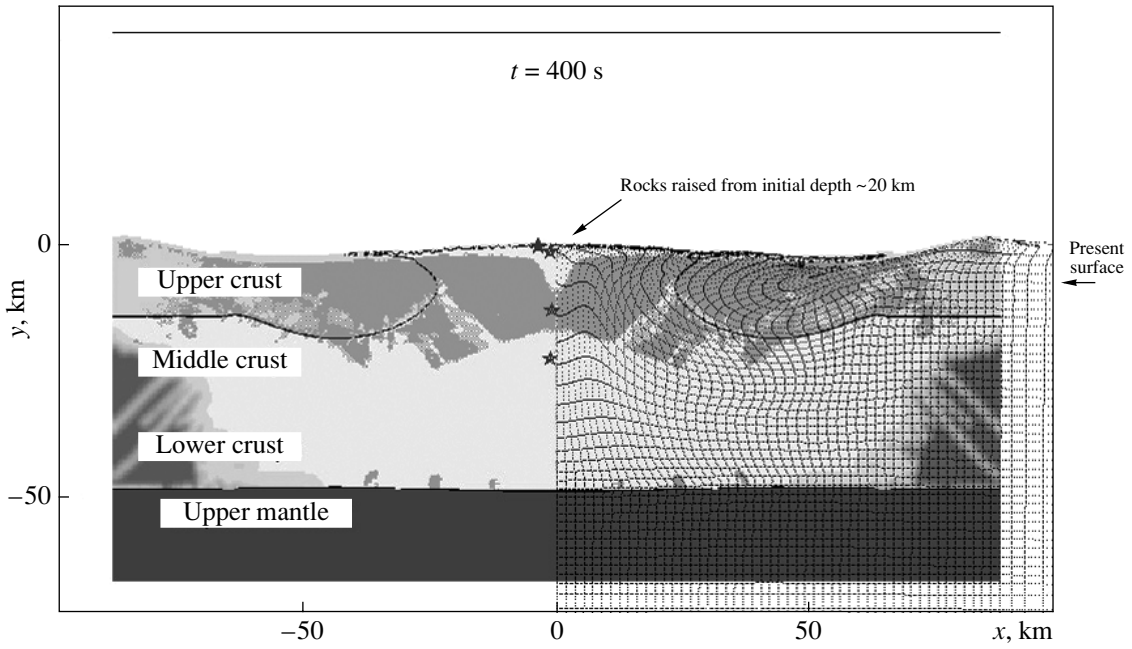

Fig. 13. Cross section of one of the model Vredefort craters 400 s after the impact. The shade of dark gray in the bottom part denotes the mantle rocks; the dark peripheral zones within the crust correspond to the boundary of the destruction zone near which individual cracks are seen. The shade of gray against the lighter background near the crater surface corresponds to the computational cells in which the internal friction was reduced at the current time step with acoustic fluidization. The intricately bent boundary of the granite crustal layer and the 14-km-thick horizontal layer of metamorphized sedimentary and igneous rocks is shown. The deformation of the initially rectangular grid of tracers constructed from the markers located initially in each fifth row and in each fifth column of the computational grid cells is shown in the right half of the figure.

acteristic thickness of the melt sheet within the crater (at the initial rock density) is estimated to be 400–800 m.

The overall scenario for the crater formation through the collapse of the transient cavity and the subsequent collapse of the central peak is generally similar to that described above for the Popigai model crater. Figure 14 shows the crater formation scenario with the distribution of the hottest material (above 800 K) highlighted by the level of gray.

Figure 15 shows the distributions of basic parameters in the upper 15 km of rocks beneath the formed crater. This range of depths most likely also includes the observed erosion level. The depth isolines of rock layers, which are horizontal in the original deposit, are shown in all panels of Fig. 15 (a, b, c). Since the vertical coordinate in the model increases from the bottom upward, the initial depth is negative. Figure 15a shows the temperature distribution in the target. The vertical lines indicate the temperatures of the postimpact thermal metamorphism observed on the visible surface corresponding to the present erosion cut estimated from mineralogical data (Foya *et al.*, 1999; Gibson and Reimold, 1998; 1999a; Gibson *et al.*, 1998). We see that the assumption about the erosion cut at 7–9 km yields good agreement between the computed and estimated (from geological data) temperatures. A characteristic feature of the model is the "inverted" thermal profile immediately after the crater formation: hotter rocks proved to be closer to the surface, as suggested by the flow pattern schematically shown in Fig. 14. Below, we show that, while cooling down, the upper hot layers heat up the rocks at a depth of 7–9 km by 100–150 K above the level indicated in Fig. 15a. This late rock heating at the present erosion cut depends on the contribution of the hydrothermal heat flux from several upper kilometers of rocks that could have a significant permeability (Abramov and Kring, 2004). Thus, a current analysis of the accuracy of the model and the geological temperature estimates can form the basis for the next iteration that would refine the possible crater formation scenarios.

Figure 15b shows the uplift/subsidence of the target layers that were originally deposited at different depths. Assuming, based on the temperature data (Fig. 15a), that the depth of the erosion cut is ~8 km, we can trace the model structure of the central uplift on the present surface. The rocks of the lower crust (the initial depth is more than 28 km) in the model are at a present depth of 2–3 km at a distance of ~5 km from the center. It should be noted that the numerical solutions at small distances from the axis are very unstable due to axial symmetry; therefore, the structure of the central part of the uplift changed over a wide range in various computations. The rocks of the middle granitoid layer (ILG rocks) from depths of more than 20–21 km were lifted to the surface and are at distances as large as 12–13 km from

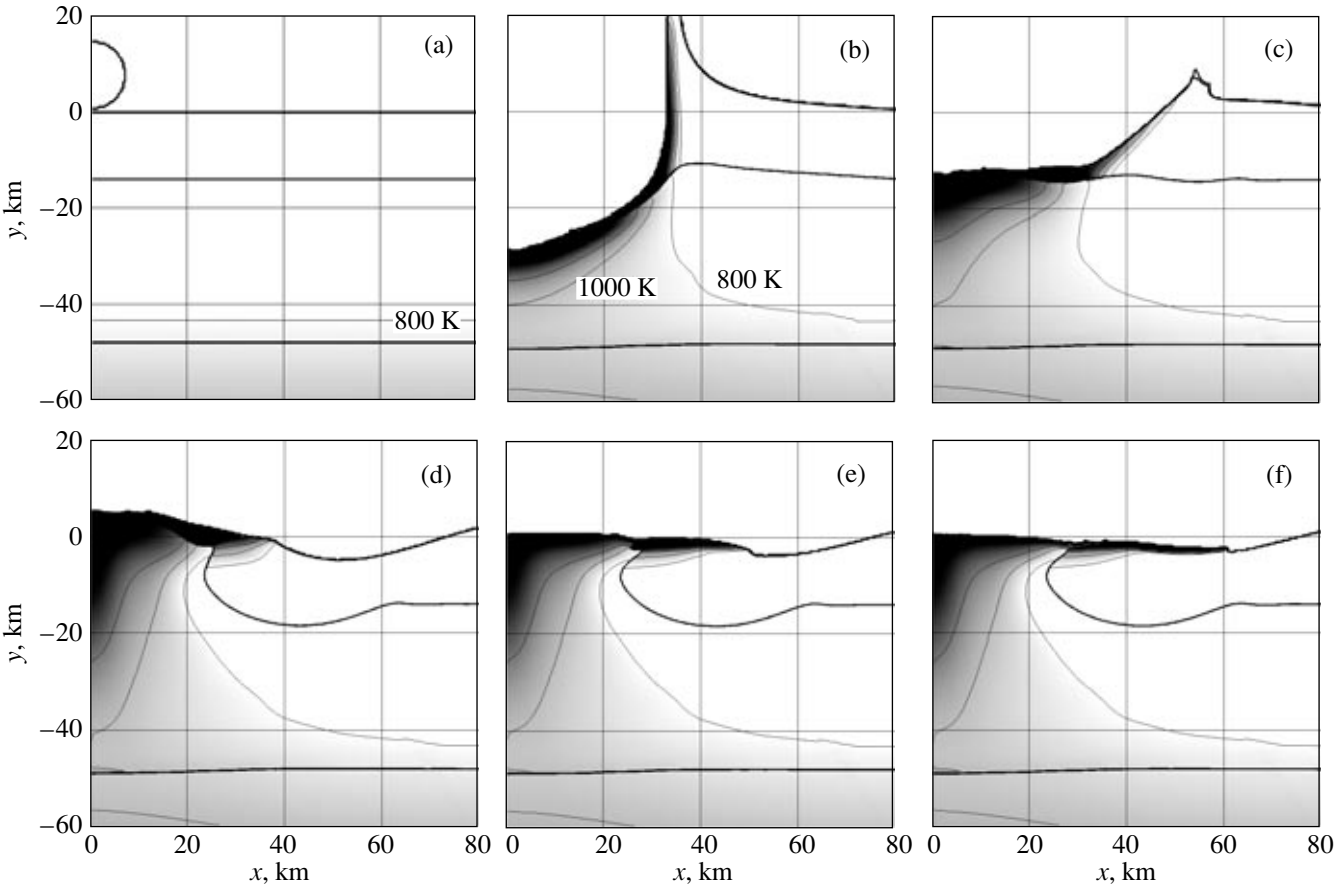

Fig. 14. Formation sequence of the model Vredefort crater with displayed rock temperatures. The shades of gray indicate the temperature distribution from 800 K or lower (light shade) to 2000 K (dark shade). For a clearer perception, the 800, 1000, and 1200 K isotherms are shown. Thus, the darkest shade gives an idea of the melt distribution in the growing crater: (a) initial position (the 800 K isotherm is horizontal, the incoming spherical projectile is seen above the target); (b) 30 s; (c) 90 s; (d) 240 s; (e) 300 s; (f) 360 s.

the center on the present model surface. Immediately after the crater formation, the temperature in these rocks was 1200 K or higher, approaching the melting temperature on the axis. The uplifted rocks in the central zone underwent initial shock compression to pressures of 40–50 GPa (Fig. 15c). Since the initial temperature of these rocks (for the geothermal gradient adopted in the model) was ~600 K (in several cases with a slightly larger temperature gradient, 700 K), the combined effect of the shock and the lifting with slight adiabatic cooling increased the temperature of these rocks by 500 K. The surface of the granitoid layer specified at a depth of 14 km approaches almost vertically the level of the presumed cut at a distance of ~23 km from the center, which is slightly larger than that observed on the terrain (~20 km, see Fig. 12); this may be considered to be a good coincidence for the fairly crude model used. Since no less deep layers were clearly distinguished in the computation, an inverse approach can be used here. Figure 15b shows that to roughly reproduce the change of rocks in the collar of the Vredefort dome (Fig. 12), we must assume that the rocks of the Witwatersrand group were deposited at depths from 7 to 10 km. If the ring fold of the rocks immersed during the crater collapse were identified with the Potchefstroom trough described for Vredefort, then the radii of the model fold (45–50 km, depending on the erosion level) and the observed trough zone (Fig. 12) would also be similar.

According to the model, the rocks in the trough zone at the present level must have been deposited in the original target at a depth of ~2 km. A direct comparison with observations is complicated by the fact that the layers of the original actual target were not horizontal (Lana *et al.*, 2003b). This gives hope that it will be possible to construct a more accurate model for comparison with geological data in three-dimensional modeling in the future.

The pressure isolines in the shock wave shown in Fig. 15c allow the model results to be compared with another series of observations. The planar deformation features (PDFs) in minerals and the shatter cones described in the literature are observed at the present level at distances up to ~30 and ~40–45 km, respectively. For the presumed level of the erosion cut, ~8 km, rocks with a shock compression levels of 7–10 and

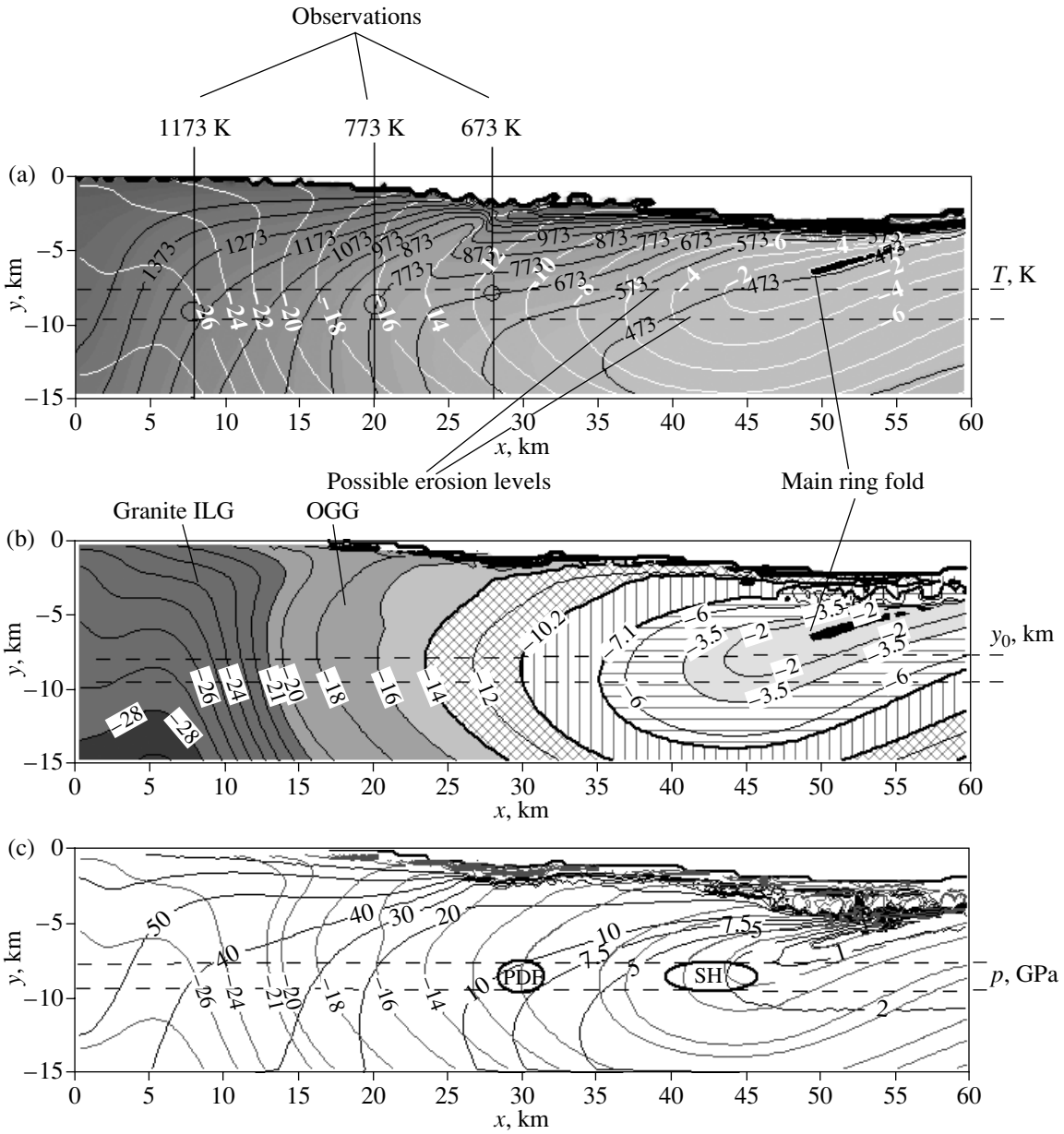

Fig. 15. Cross section of the model Vredefort crater with fields of the various parameters used to compare the model and the observations. The horizontal dotted lines at depths of ~7.5 and 9.5 km denote the expected level of the present erosion cut. The annular main fold, the place where the ejecta curtain falls back to the original target surface, is at a distance of 50 km from the center and a depth of ~6.5 km: (a) final rock temperatures. The vertical lines indicate the geological temperature estimates for the postshock rock metamorphism at the present erosion cut. The circles highlight the points of intersection between the observations and the model isotherms. The light isolines indicate the initial depth of burial of the rocks that proved to be at the final positions shown in the figure. (b) A detailed representation of the initial rock depth y_0 (in the computational grid, the y axis is directed from the bottom upward, $y = 0$ on the original surface; therefore, the depths have negative values on the isolines). Different shades of gray for depths of more than 14 km correspond to rocks of the granite crustal layer. The presumed boundary between the deeper and ancient rocks (ILG: Inlandsee Leucogranofels), with an age of 3.2–3.5 Gyr, and less deep and younger granitoid rocks (OGG: Outer Granite Gneiss), with an age of ~3.1 Gyr, is drawn at the depth of original burial, 21 km (Reimold and Gibson, 1996; Moser *et al.*, 2001). The presumed rocks of the lower crust (in the lower left corner of the figure) are bounded by the depth of burial of 28 km. The boundaries of the differently designated metamorphized sedimentary rocks buried at depths of less than 14 km are drawn in such a way that their distribution at the present erosion cut corresponds to the observations shown in Fig. 14. (c) The isobars of shock pressure in the rocks drawn at the final marker particle positions that were subjected to shock compression to the indicated pressures. The ovals indicate the observed outer boundaries of PDFs in minerals and shatter cones in rocks (SH) at distances of ~30 and 40–45 km from the center, respectively. The disordered pattern of isobars near the model crater floor reflects the mixing of tracers that recorded different shock compression levels in these zones.

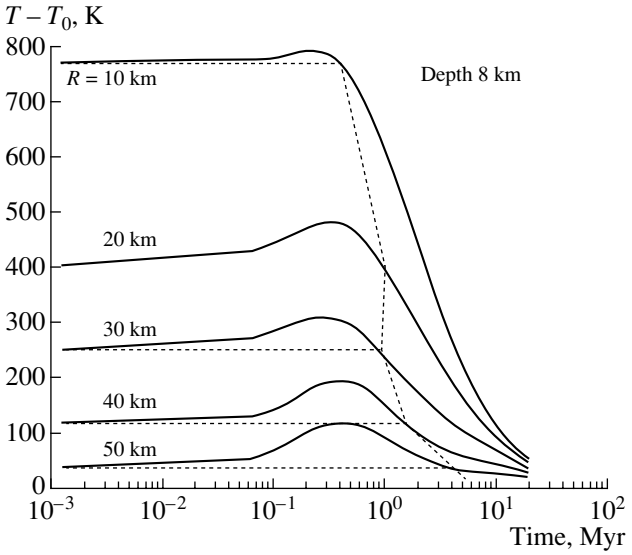

Fig. 16. Time variations in the temperature of the rocks that were at a depth of 8 km after the crater formation and that are currently on the dayside surface at the indicated radial distances from the center of the Vredefort structure. Since these rocks were covered with a layer of hotter rocks and impact melt, they were slightly heated in the first 0.5 Gyr. The cooling to the stationary temperature corresponding to the natural geothermal temperature gradient took ~10 Myr.

2–3 GPa, respectively, are located at these distances in the model. These values agree with the commonly assumed occurrence levels of PDFs in minerals and shatter cones in rocks (Stöffler and Langenhorst, 1994).

For all of the craters investigated here, we estimated the cooling rate of the rocks beneath the crater using a simple conductive heat conduction model (for details, see Ivanov, 2004b). For the Vredefort crater, the results of our modeling of the thermal evolution of the structure are shown in Fig. 16. This figure shows the temperature evolution in rocks at a depth of 8 km below the initial level of the target surface at several radial distances from the center of the structure. We see that the presence of hotter rocks below this level leads to a slight heating (by 50–100 K) with respect to the temperatures reached by the end of the crater formation. The temperatures at a depth of 8 km in the first several hundred million years slightly increase and, passing through their maximum, pass through their initial values 0.5–2 Myr later. The temperatures at a depth of 8 km 20 Myr later correspond, within 50 K, to the regional geothermal gradient.

Thus, in several relatively independent parameters (the rock temperature, the level of shock metamorphism, and the depths of original burial), the numerical model with a presumed projectile 14 km in diameter at a speed of 15 km/s is in good agreement with the geological and geophysical data. A joint analysis of the model and observational data provides a good basis for the necessary next iteration in the description of the Vredefort crater. This analysis is of great interest in discussing the possible relationship to the formation and evolution of the gold fields in the Witwatersrand basin, which constitute up to 40% of the world's gold reserves (Gibson and Reimold, 1999b).

The Sudbury impact structure with an age of 1.85 Gyr (Krogh *et al.*, 1984), as is now believed to have been proven, is the erosion remnant of a multi-ring crater (basin) deformed significantly by later tectonic deformations.

A general geological description has been given repeatedly (see, e.g., Deutsch *et al.*, 1995; Dressler, 1984). The Sudbury Igneous Complex (SIC) together with the layer of suevites (the so-called Onaping formation) is interpreted in terms of the hypothesis about an impact origin of the structure as a body of solidified melt (Deutsch *et al.*, 1995; Grieve *et al.*, 1991). The subsequent tectonic deformations of the structure, including the body of solidified melt, led to the thrust of the southern edge of the structure on the northern edge (Milkereit *et al.*, 1994b; Shanks and Schwerdtner, 1991). The current (elliptical in plan) shape of the erosion remnants of the structure resulted from these processes. According to the Lithoprobe studies, the depth of the preserved bowl with the solidified melt of target rocks is estimated to be 6 km (Deutsch and Grieve, 1994; Milkereit *et al.*, 1994b).

Reconstruction of the original geometry of the structure (Roest and Pilkington, 1994) yields an estimate for the initial melt sheet thickness of at least 2.5 km at a diameter of about 60 km. The melt body in the central depression was covered with a layer of allogenic breccias ~3 km in thickness (Deutsch *et al.*, 1995; Grieve *et al.*, 1991). The volume of the melted rocks is estimated to be $(1–2.5) \times 10^4$ km^3. The cooling time of such a significant melt volume is long enough for the melt differentiation (Ariskin *et al.*, 1999) into more basic quartz gabbro and norites in the floor part and granophyres covering them (Naldrett and Hewins, 1984). The geothermal gradient within the Canadian shield of the surface ranges from 12 to 15 K/km at a temperature at the crust–mantle boundary (at a depth of 40–50 km) of 400–500°C or 700–800 K (Jaupart and Mareschal, 1999). At the crater formation epoch, the local geothermal gradient could be larger. In the model presented here, the temperature at the crust–mantle boundary at a depth of 49 km was assumed to be 865 K. The depth of the mantle was estimated from the current value of ~44 km (Guillou *et al.*, 1994) with allowance made for the erosion cut of about 5 km of the crust thickness.

Numerical modeling of the impact formation of the Sudbury crater and estimation of its cooling history were performed previously by Ivanov and Deutch (1999). In this paper, we performed new computations using an updated code and with improved equations of state for the materials. In view of the large uncertainty in the structure of the target in the Sudbury region, we used a simplified two-layer computational model, a

granite crust over a mantle modeled by the dunite equation of state, for a preliminary analysis.

Preliminary test computations allowed us to choose, as the first approximation, the same projectile as that for the Vredefort crater described above. Consequently, the Vredefort and Sudbury craters are assumed to have similar diameters. Below, we present our results for the impact of a spherical projectile 14 km in diameter with the granite density and a speed of 15 km/s. The kinetic energy of the projectile is 4.32×10^{23} J. The computed volume of the impact melt (at the initial granite density) is 12000 km^3, which is close to the value given above for the three-layer model of the impact that produced the Vredefort crater. The small difference probably results from small differences in the thermal regimes of the targets and slight modifications of the computational code. These differences are currently being studied.

Since the overall pattern of formation of the Sudbury crater is roughly similar to that for the cases considered above, for brevity, we give no special illustrations here. In the case considered in detail below, the crater diameter at the rim crest is 175 km, the diameter at the original surface level is 150 km, the mean depth under the original surface level is 1300 m, and the rim height is about 900 m.

Comparison of the model results for the residual rock temperature and the shock compression pressure in the case of Sudbury is complicated by the severe distortion of the original crater shape by tectonic movements and erosion. Here, we attempt to make such comparisons with great caution based on the assumptions about the origin of the various observed structures.

Based on the interpretation of the seismic sounding of the structure corroborated in part by borehole drilling results, the following crater evolution scenario was suggested (Deutsch and Grieve, 1994; Deutsch *et al.*, 1995; Dressler, 1984; Milkereit *et al.*, 1994a; 1994b; Wu *et al.*, 1995). The crater was formed as a two-ring basin with a deep central depression (similar Venusian crater structures are shown in Figs. 1 and 2). A large volume of melt, ~10^4 km^3 (which subsequently formed the main body of the igneous rocks, SIC), was in the depression about 60 km in diameter. A layer of allogenic breccias retained through fast cooling and solidification of a fairly thick (several hundred kilometers) crust of a mixture of the melt and clasts from the layer of breccias was deposited on the melt lake from above. The bulk of the impact melt covered with a blanket of breccia solidified long enough for the differentiation into a heavy, refractory lower layer of norites and a less dense layer of granophyres. The region of the shield in which the crater was formed proved to be near the front of the Grenville compression (from southeast to northwest) even before the melt completely solidified. The still hot (and, hence, plastic) rocks around the crater formed a giant fold in which the southeastern rim of the crater was thrust on the collapsed northern rim. The full displacement of the southeastern rim in the form of a giant thrust by 30 km gave an oval shape to the originally circular crater. The subsequent erosion of rocks to a depth of ~5 km gave the observed shape to the remnants of the crater structure. Its impact origin can still be judged by the halos of shatter cones and the rocks with PDFs in quartz and plagioclase whose boundaries are, respectively, at 10 and 20 km from the boundary of the body of solidified melt along the present surface (Deutsch and Grieve, 1994).

This generalized scenario has many "weak" assumptions that need a further study. For example, note the unsolved (in our view) problem of the stability of a kilometer-thick layer of clastic material on the surface of a melt lake ~60 km in diameter. There are geochemical constraints on the possibility of representing the equilibrium mineral composition of the rock that can give the observed differentiates (Ariskin *et al.*, 1999). Solving this problem may require assuming the presence of contrasting (in mineral composition) rocks in the impact melt zone from the outset. Nevertheless, the scenario described above makes it possible to formulate a number of useful testable hypotheses.

For example, if we follow the idea of melt differentiation, then we must assume that the boundary between norites (below) and granophyres (above) was initially horizontal, since the differentiation took place in the field of gravity. The revealed tilt of this boundary at the northern margin of the structure, 20°–30° to the horizon, should then be attributed to the overall rotation of the block 10–30 km in diameter (from 1/4 to 1/3 of the crust thickness). This picture, in the form of the formation of a giant thrust fold, was suggested and substantiated by Wu *et al.* (1995).

Figure 17 compares the numerical model with a sketch of the profile of the structure in the north–south direction constructed from LITHOPROBE data (Milkereit *et al.*, 1994a). In the approached described above, the observed profile is rotated through 23°, which makes the boundary between norites and granophyres almost horizontal. Strictly speaking, this rotation has a meaning only for the region of the northern margin.

In Fig. 17a, the contours of the melt zone were roughly fitted to the location of the computed 1573 K (1200°C) isotherm as an approximate estimate of the melt location in the central part of the computed crater. This is supported in Fig. 17b by comparison of the observed (rotated) profile with the location of the 50 GPa isobar of shock compression pressure corresponding to the melting of granite during decompression. With this fitting of the model to the observations, the foot of the melt zone is at a depth of ~4 km relative to the original target level. If the more or less uniformly rotated block of rocks including the northern margin extends to another 10–20 km from the northern SIC boundary, the plane of the present erosion level must then go deep into the target with increasing distance from the center, as shown by the inclined dotted line in Fig. 17a. A proper comparison of the rock parameters

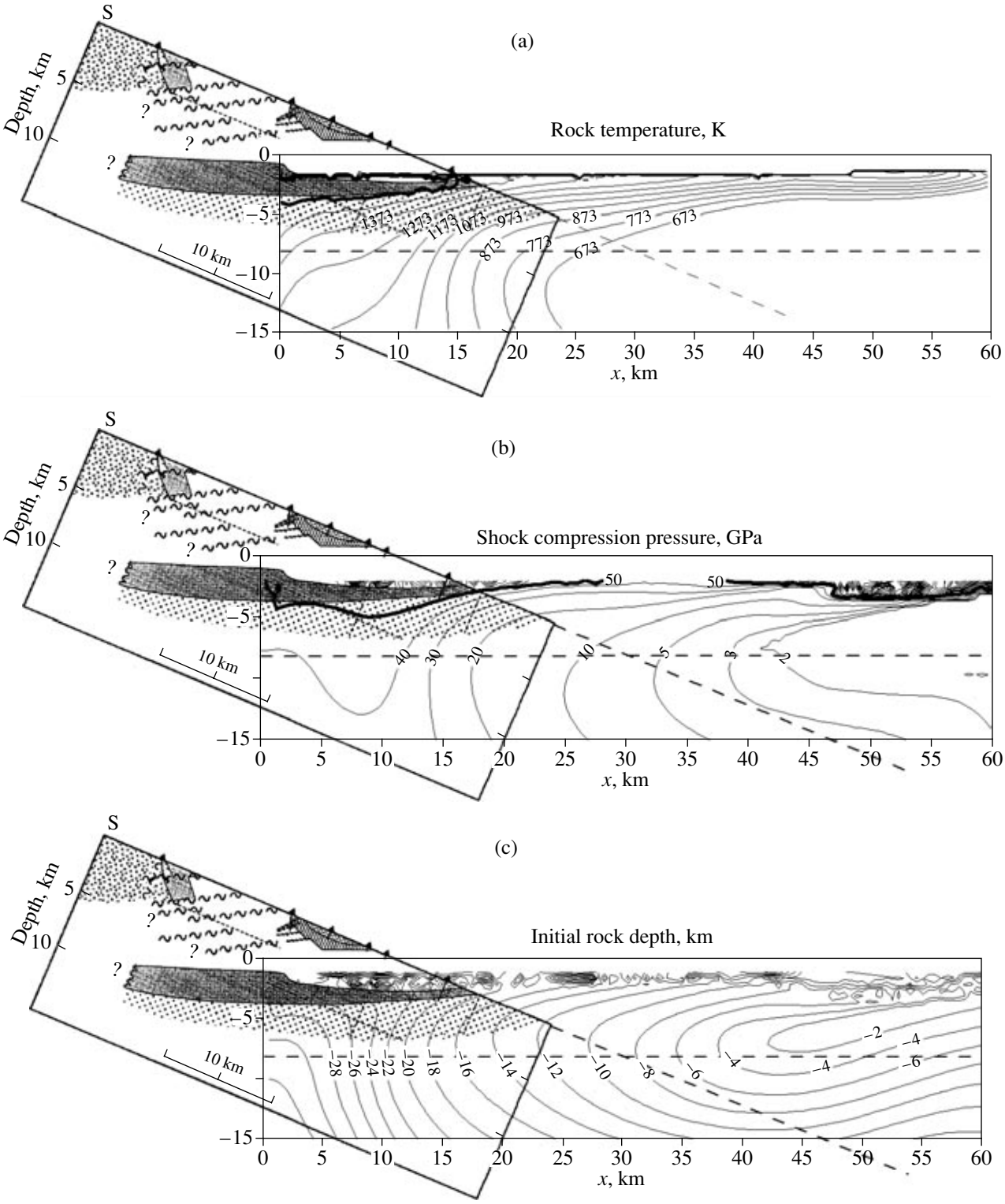

Fig. 17. (a) Temperature, (b) shock pressure, and (c) initial rock depth fields for the model Sudbury crater. A portion of the present crater profile constructed from LITHOPROBE data (Milkereit *et al.*, 1994a; 1994b; Wu *et al.*, 1995) was used for comparison with the observations. This portion was rotated through 23° clockwise by assuming that the boundary between the heavier and lighter melts (norites and granophyres) was initially horizontal (an equipotential surface in the field of gravity). An approximate alignment with the model profile was made using the 1500 K isotherm and the 50 GPa isobar that roughly bounds the impact melt zone in the model. The inclined dotted line indicates the location of the present surface within the inclined block including the northern edge of the SIC. For comparison, the horizontal dotted line indicates an approximate erosion level for Vredefort.

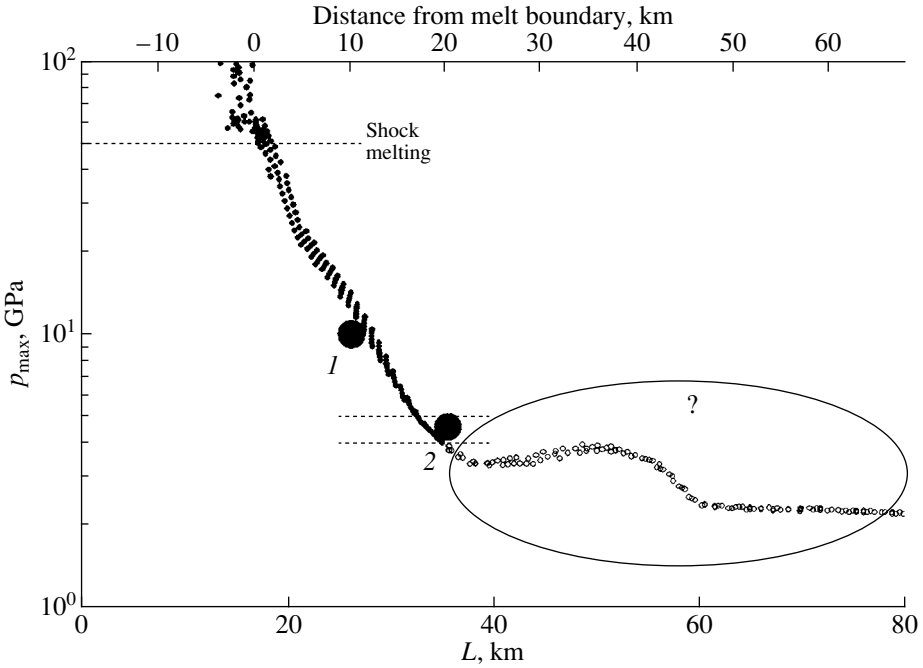

Fig. 18. Maximum shock pressure in the tracers that proved to be at the final positions at (±500 m) from the presumed present erosion surface in the rotated crustal block included the northern edge of the SIC (see Fig. 17). The filled circles correspond to the boundaries of PDFs in quartz and plagioclase (*1*) and shatter cones in rocks (*2*) observed on the present dayside surface. The ellipse with a question mark pertains to the extension of the inclined present surface at large distances where the assumption about the rotation of the crustal block as a single entity is inapplicable; the next, possibly also inclined block is most likely located at these distances.

in the model and on the terrain should then be made along this inclined line.

Figure 17c shows the lines of equal initial rock depth in the model. It follows from the comparison of the model with the observations that the rocks lifted from depths of 12–16 km are located on the surface behind the SIC margin. Their temperature immediately after the crater formation decreased from the melting temperature (at the boundary of the melt zone) to about 600°C at a distance of ~5 km.

Figure 18 shows the decrease in the shock pressures "recorded" by the tracers whose final locations are within ±0.5 km of the presumed plane of the present target surface with increasing distance from the center. The distance on the lower axis is measured from the intersection of this plane with the original target surface (at a distance of 11 km from the center); the distance on the upper axis is measured from the boundary of the melt zone (a shock pressure of ~50 GPa). This profile can be traced in Fig. 17b. Dots *1* and *2* in Fig. 18 correspond to the typical distances from the edge of the melt zone of 10 km for a shock pressure of ~10 GPa (the emergence of PDFs in quartz and plagioclase) and 20 km for a shock pressure of ~5 GPa (the emergence of shatter cones in rocks) given in the literature (Deutsch and Grieve, 1994; Grieve and Therriault, 2000). We see that the model computations are consistent with the few results for the shock pressure estimation in rocks around the Sudbury structure up to distances of ~20 km from the boundary of the melt zone. Following along the presumed inclined surface too far from the crater could be careless due to the limited sizes of the block that rotates as a single entity. If the model described above is valid, then the passage to the next block is most probable as one recedes from the SIC edge. The systems of cracks north of the SIC, which are often interpreted as the ring faults around the multi-ring structure, the first of which is at a distance of ~45 km from the center of the Sudbury basin, can be assumed to be the boundaries of the blocks (Spray *et al.*, 2004).

It should be noted that for the mutual arrangement of the presumed inclined surface and the isobars shown in Fig. 17b, the positions of the points in Fig. 18 depend weakly on the horizontal displacement of the observed crater profile rotated through 23°. For example, from the standpoint of the comparison shown in Fig. 18, the picture for the intersection of the presumed inclined surface with the original level of the model target at distances of 13–15 km from the center is approximately the same as that for the intersection at 11 km that was assumed when constructing these figures. Note also that the above comparisons pertain to a roughly diametrical profile of the Sudbury basin. The actual three-dimensional basin deformation scheme at the assumed tectonic compression still awaits a detailed development.

Thus, the assumption that Sudbury and Vredefort had a diameter of less than 200 km is consistent (in the model of a vertical impact) with the main observations known from published data.

DISCUSSION

We numerically modeled the formation of the four largest craters on the Earth. Using the same numerical model in all cases to analyze the computational and observational data allows us, on the one hand, to check where the model is valid and, on the other hand, to form a basis for generalizing the observational data collected for various impact structures variously modified by the endogenic processes of tectonics, erosion, and sedimentation. In general, it can be stated that in all of the cases considered, the model agrees satisfactorily with the observations at appropriately chosen parameters.

As follows from the model, the final shape of the impact craters is the result of the growth of a deep transient cavity, its collapse in the field of gravity with the formation of an uplift, and the subsequent collapse of the uplift with an intense flow of material over the surface of the forming crater. When the uplift is formed, the floor of the transient cavity covered with the most strongly fragmented and melted material becomes the uplift surface. When the uplift collapses, the hottest surface layers begin to flow down the slopes of the uplift, because the collapse of the uplift itself in the field of gravity is slowed down by internal friction in broken, but not melted rocks. The inner ring uplift in the model is formed by these near-surface motions of the material.

Such a cratering process is possible only when the possibility of a temporary reduction in friction in the fractured rocks surrounding the growing crater is introduced into the model. The reduction in friction can be described in terms of the acoustic fluidization model (Melosh and Ivanov, 1999). The true causes of the temporary reduction in friction may well be different, but so far the acoustic fluidization model can be considered as a convenient phenomenological model for the reduction in friction in the rocks around the crater to 0.5–0.1 followed by an exponential (in time) return of the coefficient of internal friction to its normal values of ~0.5 (corrected for the reduction in friction as the rock melting point is approached). To reproduce the observed shapes of the final flattened craters, we must assume that the characteristic friction restoration time (in the time-exponential relation) to a normal coefficient of friction in the rocks beneath the craters is 90–100 s for the Popigai crater and 120–160 s for the other craters. These values can probably be used to model large meteorite craters on other planets. More detailed modeling of a wide range of crater diameters suggests that the decay time in the acoustic fluidization model is approximately proportional to the projectile diameter at the same speed of the projectiles in events of different scales (Wünnemann and Ivanov, 2003).

From the standpoint of modeling, the formation of a complex meteorite crater described above creates great difficulties for reproducing the observed crater depth. At the excavation phase of the transient cavity, the rocks beneath the impact center are displaced downward by 20–30 km and then, during its collapse, rise by 5–10 km above the original surface layer and, at the end, sink to the final location by 1–2 km below the original surface layer. At a vertical displacement amplitude of 30–40 km, it is hard to find a set of model parameters that would ensure the stop at the position corresponding to the observations. Therefore, caution should be exercised in treating the results of the computations for a detailed model crater profile. We cannot rule out the possibility that introducing a more perfect description of the behavior of large masses of fractures rocks into the model will require choosing the basic parameters again.

The spatial resolution of the model is a separate problem. A careful computation of the shock wave and its attenuation in the target requires that the projectile be covered with a grid of computational cells with a resolution of at least ~40 cells for the projectile diameter. At a projectile diameter of 10–15 km, this implies that the spatial step of the computational grid must be no more than 200–300 m. A finer grid step would lead to a rapid increase in computational time. The commonly used grid coarsening technique after the completion of the phase of the shock passage through the computational region is inapplicable in the problem under consideration, because at the final formation phase of a flat crater with a diameter of 100–200 km and a depth of ~1 km, even cells with a diameter of 100 m are too large to trust the computational results with regard to reproducing the relief of the crater floors. A further development of the model must probably follow the path of successively solving the problem on different grids specially constructed for each phase of the process with a successive reinterpolation of the current results. This is particularly necessary when passing to three-dimensional computations in the near future, where it is even more difficult to maintain the balance between the spatial resolution and the computational time.

Our computations also revealed other, as yet unsolved problems. One of these is a significant wall height obtained in most computations. Figure 19 compares the profiles for the Stanton crater on Venus and one of the computations (a projectile 14 km in diameter at an impact velocity of 12 km/s). We see that with the profiles being generally similar, the rim height for the model crater is about 1300 m, while no such rim is detected in the Magellan height profiles. No high rim was observed in the computations by O'Keefe and Ahrens (1999), where the collapse of the transient crater was ensured by the assumption about a low rock strength (instead of the acoustic fluidization model used in this paper). This serious disagreement between the model and the observations undoubtedly requires a further analysis.

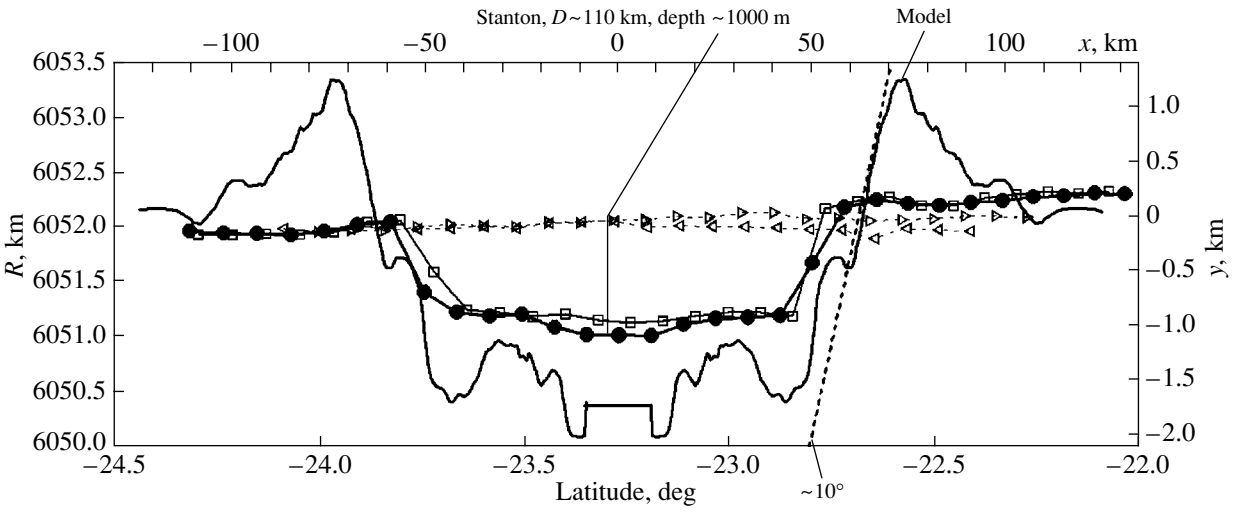

Fig. 19. Comparison of the profile for the Venusian Stanton crater constructed from Magellan radio-altimetric data with the model crater produced in a target similar to the target of the Vredefort crater by the impact of a spherical asteroid 14 km in diameter at a speed of 12 km/s. Note the presence of a high rim around the model crater. The notation on the profiles of the Venusian crater is the same as that in Fig. 2. The inclined dotted line indicates the mean slope angle of the model crater, ~10° (the static coefficient of friction in the fragmented material of the target was about 0.5).

In conclusion, returning to one of our goals, the development of approaches to modeling the formation of lunar impact basins, we note that, in some measure, this paper does not give an unambiguous answer to the question of whether the largest terrestrial impact structures can be considered as analogues of lunar basins. The suggested model for the formation of terrestrial craters in comparison with the observational data describes their formation as morphologically complex craters with a central uplift of deep rocks at the crater center by 12–25 km, which is about 1/10 of the crater diameter. This corresponds to the relationships derived previously from purely geological considerations (Grieve *et al.*, 1981). At the same time, the model does not reproduce any additional formation mechanisms of many rings typical of lunar basins. In our opinion, among the possible factors that determine this difference, two assumptions primarily deserve a study: first, the relationship between the diameter of structures and the crust thickness differs from that on the Earth; and, second, since all impact basins on the Moon are older than 3.7–3.8 Gyr, it is necessary to take into account the thermal gradient, which for the young Moon was much higher than that at present. These assumptions will be used as the basis for further studies.

CONCLUSIONS

The results of our numerical modeling of the formation of the largest terrestrial craters presented here allowed us to make a detailed comparison with available geological and geophysical data. We found agreement in such parameters as the crater morphology and depth, the impact melt volume, and the distribution of shock pressures and temperatures in the rocks beneath the crater. The model parameters for the mechanical behavior of rocks chosen from the conditions for the best agreement between the computations and the available observations can be used to study the cratering processes on other planets, including the most interesting (for the geological history of the Moon) giant impact basins.

ACKNOWLEDGMENTS

I wish to thank V.N. Zharkov and V.L. Masaitis for reviews that contributed to the significant improvement of the manuscript. This work was supported by the Russian Foundation for Basic Research (project no. 04-05-64338).

REFERENCES

Abramov, O. and Kring, D.A., Numerical Modeling of an Impact-Induced Hydrothermal System at the Sudbury Crater, *J. Geophys. Res. (Planets)*, 2004, vol. 109, p. 10007.

Alvarez, L.W., Alvarez, W., Asaro, F., *et al.*, Extraterrestrial Cause for the Cretaceous-Tertiary Extinction, *Science*, 1980, vol. 208, pp. 1095–1108.

Amsden, A.A., Ruppel, H.M., and Hirt, C.W., *SALE: A Simplified ALE Computer Program for Fluid Flow at All Speeds*, Los Alamos: Los Alamos Laboratory Report LA-8095, 1980.

Ariskin, A.A., Deutsch, A., and Ostermann, M., Sudbury Igneous Complex: Simulating Phase Equilibria and in Situ Differentiation for Two Proposed Parental Magmas, in *Large Meteorite Impacts and Planetary Evolution II*, Dressler, B.O., and Sharpton, V.L., Eds., Boulder: Geological Soc. Am., 1999, pp. 373–387.

Barsukov, V.L., Venusian Igneous Rocks, in *Venus geology, geochemistry, and geophysics—Research results from the USSR*, Barsukov, V.L., Basilevsky, A.T., Volkov, V.P., *et al.*, Eds., Tucson: Univ. Arizona Press, 1992, pp. 165–176.

Bottomley, R., Grieve, R., York, D., *et al.*, The Age of the Popigai Impact Event and Its Relation To Events at the Eocene/Oligocene Boundary, *Nature*, 1997, vol. 388, pp. 365–368.

Bralower, T.J., Paull, C.K., and Leckie, R.M., The Cretaceous-Tertiary Boundary Cocktail: Chicxulub Impact Triggers Margin Collapse, *Geology*, 1998, vol. 26, no. 4, pp. 331–334.

Christeson, G.L., Nakamura, Y., Buffler, R.T., *et al.*, Deep Crustal Structure of the Chicxulub Impact Crater, *J. Geophys. Res.*, 2001, vol. 106, pp. 21751–21770.

Collins, G.S., Melosh, H.J., and Ivanov, B.A., Modeling Damage and Deformation in Impact Simulations, *Met. Plan. Sci*, 2004, vol. 39, no. 2, pp. 217–231.

Dahlman, O. and Israelson, H., *Monitoring Underground Nuclear Explosions*, New York: Elsevier, 1977.

De Wit, M.J., Roering, C., Hart, R.J., *et al.*, Formation of An Archean Continent, *Nature*, 1992, vol. 357, pp. 553–562.

Deutsch, A. and Grieve, R.A.F., The Sudbury Structure: Constraints on Its Genesis from Lithoprobe Results, *Geophys. Res. Lett.*, 1994, vol. 21, pp. 963–966.

Deutsch, A., Grieve, R.A.F., Avermann, M., *et al.*, The Sudbury Structure (Ontario, Canada): a Tectonically Deformed Multi-Ring Impact Basin, *Geol. Rundsch.*, 1995, vol. 84, no. 4, pp. 697–709.

Deutsch, A., Masaitis, V.L., Langenhorst, F., *et al.*, Popigai, Siberia-Well Preserved Giant Impact Structure, National Treasury, and World'S Geological Heritage, *Episodes*, 2000, vol. 23, no. 1, pp. 3–11.

Dines, J. and Walsh, J., Impact Theory: General Principles and Method of Calculation in Euler Coordinates, in *Vysokoskorostnye udarnye yavleniya* (High-Speed Impact Phenomena), Moscow: Mir, 1973, pp. 49–111.

Donofrio, R.R., North American Impact Structures Hold Giant Field Potential, *Oil Gas J.*, 1998, no. 5, pp. 69–83.

Doucoure, C.M., de Wit, M.J., and Mushayandebvu, M.F., Effective Elastic Thickness of the Continental Lithosphere in South Africa, *J. Geophys. Res.*, 1996, vol. 101, pp. 11291–11304.

Dressler, B.O., General Geology of the Sudbury Area, in *The Geology and Ore Deposits of the Sudbury Structure: Ontario Geological Survey Special*, Pye, E.G., Naldrett, A.J., and Giblin, P.E., Eds., Ontario: Ministry of Natural Resoursec of Canada, 1984, vol. 1, pp. 57–82.

Dutta, U., Biswas, N., Martirosyan, A., *et al.*, Estimation of Earthquake Source Parameters and Site Response in Anchorage, Alaska from Strong-Motion Network Data Using Generalized Inversion Method, *Phys. Earth, Planet. Inter.*, 2003, vol. 137, pp. 13–29.

Ebbing, J., Janle, P., Koulouris, J., *et al.*, 3D Gravity Modelling of the Chicxulub Impact Structure, *Planet. Space Sci.*, 2001, vol. 49, pp. 599–609.

Foya, S.N., Gibson, R.L., and Reimold, W.U., Impact-Related Hydrothermal Alteration of Witwatersrand Gold Reefs in the Vredefort Dome and Witwatersrand Goldfields, South Africa, *Met. Plan. Sci.*, 1999, vol. 34 (Suppl.), p. 37.

Gibson, R.L. and Reimold, W.U., Thermal Metamorphic Signature of An Impact Event in the Vredefort Dome, South Africa, *Geology*, 1998, vol. 26, no. 9, pp. 787–790.

Gibson, R.L., Reimold, W.U., and Stevens, G., Impact-Related Metamorphism in the Vredefort Dome, South Africa, in *29th Lunar and Planet. Sci. Conf.*, 1998, Abstract #1360.

Gibson, R.L. and Reimold, W.U., The Metamorphic Fingerprint of Large Impact Events: The Example of the Vredefort Dome, South Africa, *Met. Plan. Sci.*, 1999a, vol. 34 (Suppl.), p. 42.

Gibson, R.L. and Reimold, W.U., The Significance of the Vredefort Dome for the Thermal and Structural Evolution of the Witwatersrand Basin, South Africa, *Mineral. Pertol.*, 1999b, vol. 66, pp. 5–23.

Gibson, R.L. and Jones, M.Q.W., Late Archean to Paleoproterozoic Geotherms in the Kaapvaal Craton, South Africa: Constraints on the Thermal Evolution of the Witwatersrand Basin, *Basin Res.*, 2002, vol. 14, pp. 169–181.

Grajales-Nishimura, J.M., Cedillo-Pardo, E., Rosales-Dominguez, C., *et al.*, Chicxulub Impact: The Origin of Reservoir and Seal Facies in the Southeastern Mexico Oil Fields, *Geology*, 2000, vol. 28, pp. 307–310.

Grieve, R.A.F., Robertson, P.B., and Dence, M.R., Constraints on the Formation of the Ring Impact Structures, in *Multiring Basins*, Schultz, P.H. and Merrill, R.B., Eds., New York: Pergamon, 1981, pp. 37–57.

Grieve, R.A.F., Stöffler, D., and Deutsch, A., The Sudbury Structure: Controversial or Misunderstood?, *J. Geophys. Res.*, 1991, vol. 96, pp. 22753–22764.

Grieve, R.A.F. and Cintala, M.J., An Analysis of Differential Impact Melt-Crater Scaling and Implications for the Terrestrial Impact Record, *Meteoritics*, 1992, vol. 27, pp. 526–538.

Grieve, R.A.F. and Cintala, M.J., Planetary Differences in Impact Melting, *Adv. Space Res.*, 1997, vol. 20, pp. 1551–1560.

Grieve, R. and Therriault, A., Vredefort, Sudbury, Chicxulub: Three of a Kind?, *Ann. Rev. Earth Planet. Sci.*, 2000, vol. 28, pp. 305–338.

Guillou, L., Mareschal, J.-C., Jaupart, C., *et al.*, Heat Flow, Gravity and Structure of the Abitibi Belt, Superior Province, Canada: Implications for Mantle Heat Flow, *Tectonophysics*, 1994, vol. 122, pp. 103–123.

Gupta, S.C., Ahrens, T.J., and Yang, W., Shock Induced Vaporization of Anhydrite $CaSO_4$ and Calcite $CaCO_3$, in *APS Meeting Abstracts*, 1999.

Henkel, H. and Reimold, W.U., Geophysical Modeling and Reconstruction of the Vredefort Impact Structure, South Africa, *Met. Plan. Sci.*, 1996, vol. 31, p. 59.

Hildebrand, A.R., Penfield, G.T., Kring, D.A., *et al.*, Chicxulub Crater: A Possible Cretaceous-Tertiary Boundary Impact Crater on the Yucatan Peninsula, *Geology*, 1991, vol. 19, pp. 867–871.

Ivanov, B.A., Bazilevskii, A.T., Krivchkov, V.P., *et al.*, Impact Craters of Venus—Analysis of *Venera 15* and *16* Data, *J. Geophys. Res.*, 1986, vol. 91, pp. 413–430.

Ivanov, B.A., The Morphometry of Impact Craters on Venus, *Astron. Vestn.*, 1989, vol. 23, no. 1, pp. 39–49.

Ivanov, B.A., Nemchinov, I.V., Svetsov, V.A., *et al.*, Impact Cratering on Venus: Physical and Mechanical Models, *J. Geophys. Res. E*, 1992, vol. 97, no. 10, pp. 16167–16181.

Ivanov, B.A. and Ford, P.G., The Depths of the Largest Impact Craters on Venus, *24th Lunar and Planet. Sci. Conf.*, 1993, pp. 689–690.

Ivanov, B.A., Badukov, D.D., Yakovlev, O.I., *et al.*, Degassing of Sedimentary Rocks Due to Chicxulub Impact:Hydrocode and Physical Simulations, *Geol. Soc. Spec. Pap.*, 1996, vol. 307, pp. 125–139.

Ivanov, B.A., Basilevsky, A.T., and Neukum, G., Atmospheric Entry of Large Meteoroids: Implication To Titan, *Planet. Space Sci.*, 1997, vol. 45, pp. 993–1007.

Ivanov, B.A. and Deutsch, A., Sudbury Impact Event: Cratering Mechanics and Thermal History, in *Large Meteorite Impacts and Planetary Evolution II*, Dressler, B., and Sharpton, V.L., Eds., Boulder: Geological Soc. Am., 1999, pp. 389–397.

Ivanov, B.A., Large Impact Crater Modeling: Chicxulub, *Third International Conference on Large Meteorite Impacts, Nordlingen, Germany, 2003*, Houston: Lunar Planet. Inst., 2003a, Abstract #4067; http://www.lpi.usra.edu/meetings/largeimpacts2003/pdf/4067.pdf.

Ivanov, B.A., Modification of ANEOS for Rocks in Compression, *Impact Cratering: Bridging the Gap Between Modeling and Observations, February, LPI Contrib., no. 1155, 2003*, Houston: Lunar Planet. Inst., 2003b, p. 40.

Ivanov, B., Multi-Ring Basins: Modeling Terrestrial Analogs, *40th Vernadsky/Brown Microsymposium on Comparative Planetology, Moscow, 2004*, Moscow: Vernadsky Institute, 2004a, CD-ROM #30.

Ivanov, B.A., Heating of the Lithosphere during Meteorite Cratering, *Astron. Vestn.*, 2004b, vol. 38, no. 4, pp. 304–318 [*Sol. Syst. Res.* (Engl. Transl.), vol. 38, no. 4, p. 266–279].

Ivanov, B.A., Langenhorst, F., Deutsch, A., *et al.*, Anhydrite EOS and Phase Diagram in Relation To Shock Decomposition, *35th Lunar and Planet. Sci. Conf.*, 2004, Abstract #1489.

Ivanov, B.A., Shock Melting of Permafrost on Mars: Water Ice Multiphase Equation of State for Numerical Modeling and Its Testing, *Lunar and Planet. Sci. Conf.*, 2005, Abstract #1232.

James, D.E. and Fouch, M.J., VanDecar J.C., *et al.*, Tectospheric Structure Beneath Southern Africa, *Geophys. Res. Lett.*, 2001, vol. 28, no. 13, pp. 2485–2488.

Jaupart, C. and Mareschal, J.C., The Thermal Structure and Thickness of Continental Roots, *Lithos*, 1999, vol. 48, pp. 93–114.

Krogh, T.E., Davis, D.W., and Corfu, F., Precise of U-Pb Zircon and Baddeleyite Ages for the Sudbury Area, in *The Geology and Ore Deposits of the Sudbury Structure*, Pye, E.G., Naldrett, A.J., and Giblin, P.E., Eds., Ontario: Ontario Geological Survay, 1984, vol. 1, pp. 431–446.

Kuznetsov, N.M., Kinetics of Shock-Wave Phase Transformation of Quartz, in *Udarnye volny i ekstremal'nye sostoyaniya veshchestva* (Shock Waves and Extreme States of Material) Fortov, V.E., Al'tshuler, L.V., Trunin, R.F., and Funtikov, A.I., Eds., Moscow: Nauka, 2000, pp. 199–218.

Lana, C., Gibson, R.L., Kisters, A.F.M., *et al.*, Archean Crustal Structure of the Kaapvaal Craton, South Africa - Evidence from the Vredefort Dome, *Tectonophysics*, 2003a, vol. 206, pp. 133–144.

Lana, C., Gibson, R.L., and Reimold, W.U., Impact Tectonics in the Core of the Vredefort Dome, South Africa: Implications for Central Uplift Formation in Very Large Impact Structures, *Met. Plan. Sci.*, 2003b, vol. 38, pp. 1093–1107.

Lana, C., Reimold, W.U., Gibson, R.L., *et al.*, Nature of the Archean Midcrust in the Core of the Vredefort Dome, Central Kaapvaal Craton, South Africa 1, *Geochim. Cosmochim. Acta*, 2004, vol. 68, pp. 623–642.

Landau, L. and Lifshits, E., *Statisticheskaya fizika* (Statistical Physics), Leningrad: Tekhniko-Teor. Literatura, 1951.

Langenhorst, F., Deutsch, A., Hornemann, U., *et al.*, On the Shock Behaviour of Anhydrite: Experimental Results and Natural Observations, *34th Lunar and Planet. Sci. Conf.*, 2003, Abstract #1638.

Masaitis, V.L., Mikhailov, M.V., and Selivanovskaya, T.V., *Popigaiskii meteoritnyi krater* (Popigai Meteorite Crater), Moscow: Nauka, 1975.

Masaitis, V.L., Danilin, A.N., Mashchak, M.S., *et al.*, *Geologiya astroblem* (Geology of Astroblemes), Leningrad: Nedra, 1980.

Masaitis, V.L. and Raikhlin, A.I., The Popigai Crater Was Formed by the Impact of an Ordinary Chondrite, *Dokl. Akad. Nauk SSSR*, 1986, vol. 286, no. 6, pp. 159–163.

Masaitis, V.L., Impactites from Popigai Crater, in *Large Meteorite Impacts and Planetary Evolution*, Grieve, R.A.F., Sharpton, V.L., and Dressler, B.O., Eds., *Geol. Soc. Am. Spec. Pap.*, 1994, vol. 293, pp. 153–162.

Masaitis, V.L., Mashchak, M.S., and Raikhlin, A.I., *et. al.*, *Almazonosnye impaktity Popigaiskoi astroblemy* (Diamond-Bearing Impactites of the Popigai Astrobleme), St. Petersburg: VSEGEYa, 1998.

Masaitis, V.L., Popigai Crater: Origin and Distribution of Diamond-Bearing Impactites, *Met. Plan. Sci.*, 1998, vol. 33, pp. 349–359.

Masaitis, V.L., Mashchak, M.S., and Naumov, M.V., Original Diameter and Depth of Erosion of the Popigai Impact Crater, Russia, *Third International Conference on Large Meteorite Impacts, Nordlingen, Germany, 2003*, Houston: Lunar Planet. Inst., 2003, Abstract #4039; http://www.lpi.usra.edu/meetings/largeimpacts2003/pdf/4039.pdf.

McKinnon, W.B., Zahnle, K.J., Ivanov, B.A., *et al.*, Cratering on Venus: Models and Observations, in *Venus II*, Bougher, S.W., Hunten, D.M., and Phillips, R.J., Eds., Tuscon: Univ. Arizona Press, 1997, pp. 969–1014.

Melosh, H.J., Ryan, E.V., and Asphaug, E., Dynamic Fragmentation in Impacts: Hydrocode Simulation of Laboratory Impacts, *J. Geophys. Res.*, 1992, vol. 97, pp. 14735–14759.

Melosh, H.J., *Impact Cratering—A Geologic Process*, New York: Oxford, 1989. Translated under the title *Udarnye kratery—geologicheskii protsess*, Moscow: Mir, 1994.

Melosh, H.J. and Ivanov, B.A., Impact Crater Collapse, *Ann. Rev. Earth Planet. Sci.*, 1999, vol. 27, pp. 385–415.

Melosh, H.J., A New and Improved Equation of State for Impact Studies, *31th Lunar and Planet. Sci. Conf.*, Houston, 2000, Abstract #1903.

Milkereit, B., Green, A., Wu, J., *et al.*, Integrated Seismic and Borehole Geophysical Study of the Sudbury Igneous Complex, *Geophys. Res. Lett.*, 1994a, vol. 21, pp. 931–934.

Milkereit, B., White, D.J., and Green, A.G., Towards an Improved Seismic Imaging Technique for Crustal Structures: The Lithoprobe Sudbury Experiment, *Geophys. Res. Lett.*, 1994b, vol. 21, pp. 927–930.

Morgan, J. and Warner, M., and the Chicxulub Working Group. Size and Morphology of the Chicxulub Impact Crater, *Nature*, 1997, vol. 390, pp. 472–476.

Morgan, J.V., Warner, M.R., Collins, G.S., *et al.*, Peak-Ring Formation in Large Impact Craters: Geophysical Constraints from Chicxulub, *Tectonophysics*, 2000, vol. 183, pp. 347–354.

Moser, D.E., Flowers, R.M., and Hart, R.J., Birth of the Kaapvaal Tectosphere 3.08 Billion Years Ago, *Science*, 2001, vol. 291, no. 5503, pp. 465–468.

Naldrett, A.J and Hewins, R.H, The Main Mass of the Sudbury Igneous Complex, in *The Geology and Ore Deposits of the Sudbury Structure: Ontario Geological Survey Special* Pye, E.G., Naldrett, A.J., and Giblin, P.E., Eds., Ontario: Ministry of Natural Resources of Canada, 1984, vol. 1, pp. 235–251.

Nguuri, T.K., Gore, J., James, D.E., *et al.*, Crustal Structure Beneath Southern Africa and Its Implications for the Formation and Evolution of the Kaapvaal and Zimbabwe Cratons, *Geophys. Res. Lett.*, 2001, vol. 28, no. 13, pp. 2502–2504.

Nikolaeva, O.V., Geochemistry of the *Venera 8* Material Demonstrates the Presence of Continental Crust on Venus, *Earth, Moon, and Planets*, 1990, vol. 50, pp. 329–341.

O'Keefe, J.D. and Ahrens, T.J., Complex Craters: Relationship of Stratigraphy and Rings To Impact Conditions, *J. Geophys. Res.*, 1999, vol. 104, pp. 27091–27104.

Papadopoulos, G.A. and Plessa, A., Magnitude-Distance Relations for Earthquake-Induced Landslides in Greece, *Engineering Geology*, 2000, vol. 58, no. 3-4, pp. 377–386.

Pierazzo, E., Vickery, A.M., and Melosh, H.J., A Reevaluation of Impact Melt Production, *Icarus*, 1997, vol. 127, pp. 408–423.

Pierazzo, E., Kring, D.A., and Melosh, H.J., Hydrocode Simulation of the Chicxulub Impact Event and the Production of Climatically Active Gases, *J. Geophys. Res.*, 1998, vol. 103, pp. 28607–28625.

Pierazzo, E. and Melosh, H.J., Hydrocode Modeling of Chicxulub as An Oblique Impact Event, *Tectonophysics*, 1999, vol. 165, pp. 163–176.

Pike, R.J., Control of Crater Morphology by Gravity and Target Type—Mars, Earth, Moon, *11th Lunar and Planet. Sci. Conf.*, New York: Pergamon, 1980, pp. 2159–2189.

Pilkington, M. and Hildebrand, A.R., Three-Dimensional Magnetic Imaging of the Chicxulub Crater, *J. Geophys. Res.*, 2000, vol. 105, pp. 23479–23492.

Pope, K.O., Baines, K.H., Ocampo, A.C., *et al.*, Impact Winter and the Cretaceous/Tertiary Extinctions: Results of a Chicxulub Asteroid Impact Model, *Tectonophysics*, 1994, vol. 128, pp. 719–725.

Pope, K.O., Baines, K.H., Ocampo, A.C., *et al.*, Energy, Volatile Production, and Climatic Effects of the Chicxulub Cretaceous/Tertiary Impact, *J. Geophys. Res.*, 1997, vol. 102, pp. 21645–21664.

Reimold, W.U. and Gibson, R.L., Geology and Evolution of the Vredefort Impact Structure, South Africa, *Afr. J. Earth Sci.*, 1996, vol. 23, no. 2, pp. 125–162.

Ricoy, V., The Cantarell Breccia System, Southern Gulf Of Mexico: Structural Evolution and Support for An Origin Related To the Chixculub Meteorite Impact, *EGS—AGU—EUG Joint Assembly*, Nice, France, 2003, Abstract #13339.

Roest, W.R. and Pilkington, M., Restoring Post-Impact Deformation at Sudbury: A Circular Argument, *Geophys. Res. Lett.*, 1994, vol. 21, pp. 959–962.

Rozen, O.M., Bibikova, E.V., and Zhuravlev, A.B., Early Crust of the Anabar Shield: Age and Formation Models, in *Rannyaya kora Zemli: sostav i vozrast* (Early Crust of the Earth: Composition and Age), Mergasov, G.G., Ed., Moscow: Nauka, 1991, pp. 199–244.

Rosen, O.M., Condie, K.C., Natapov, L.M., *et al.*, Archean and Early Proterozoic Evolution of the Siberian Craton: A Preliminary Assessment, in *Developments in Precambrian Geology*, Windley, B.F., Ed., Amsterdam: Elsevier, 1994, pp. 411–459.

Schmidt, R.M. and Housen, K.R., Some Recent Advances in the Scaling of Impact and Explosion Cratering, *Int. J. Impact Eng.*, 1987, vol. 5, pp. 543–560.

Shanks, W.S. and Schwerdtner, W.M., Crude Quantitative Estimates of the Original Northwest-Southwest Dimension of the Sudbury Structure, South Central Canadian Shield, *Can. J. Earth Sci.*, 1991, vol. 28, pp. 1677–1686.

Spray, J.G., Butler, R.F., and Thomson, L.M., Tectonic Influences on the Morphometry of the Sudbury Impact Structure: Implications for Terrestrial Cratering and Modeling, *MAPS*, 2004, vol. 31, no. 2, pp. 287–301.

Stevens, G., Armstrong, R.A., and Gibson, R.L., Pre- and Postimpact Metamorphism in the Core of the Vredefort Dome: Clues To Crustal Response at a Massive Meteorite Strike, *Met. Plan. Sci.*, 1999, vol. 34 (Suppl.), p. 112.

Stöffler, D. and Langenhorst, F., Shock Metamorphism of Quartz in Nature and Experiment: I. Basic Observation and Theory, *Meteoritics*, 1994, vol. 29, pp. 155–181.

Stöffler, D., Artemieva, N.A., Ivanov, B.F., *et al.*, Origin and Emplacement of the Impact Formations at Chicxulub, Mexico, As Revealed by the ICDP Deep Drilling at Yaxcopoil-1 and by Numerical Modeling, *Met. Plan. Sci.*, 2004, vol. 39, no. 7, pp. 1035 –1067.

Stroenie zemnoi kory Anabarskogo shchita (Structure of the Terrestrial Crust of the Anabar Shield), Moralev, V.M., Ed., Moscow: Nauka, 1986.

Surkov, Y.A. and Barsukov, V.L., Composition, Structure and Properties of Venus Rocks, *Adv. in Space Res,* 1985, vol. 5, pp. 17–29.

Swisher, C.C., Grajales-Nishimura, J.M., Montanari, A., *et al.*, Coeval $^{40}Ar/^{39}Ar$ Ages of 65.0 Million Years Ago from Chicxulub Crater Melt Rock and Cretaceous-Tertiary Boundary Tektites, *Science*, 1992, vol. 257, pp. 954–958.

Therriault, A.M., Grieve, R.A.F., and Reimold, W.U., Original Size of the Vredefort Structure: Implications for the Geological Evolution of the Witwatersrand Basin, *Met. Plan. Sci.*, 1997, vol. 32, pp. 71–77.

Thompson, S.L. and Lauson, H.S., *Improvements in the Chart-D radiation hydrodynamic code III: Revised analytical equation of state*, Albuquerque: Sandia Laboratories, 1972, SC-RR-71 0714.

Turtle, E.P. and Pierazzo, E., Constraints on the Size of the Vredefort Impact Crater from Numerical Modeling, *Met. Plan. Sci.*, 1998, vol. 33, pp. 483–490.

Turtle, E.P., Pierazzo, E., and O'Brien, D.P., Numerical Modeling of Impact Heating and Cooling of the Vredefort Impact Structure, *Met. Plan. Sci.*, 2003, vol. 38, pp. 293–303.

Wieland, F., Gibson, R.L., Reimold, W.U., *et al.*, Structural Evolution of the Central Uplift of the Vredefort Impact Structure, South Africa, *Met. Plan. Sci.*, 2003, vol. 38 (Suppl.), p. 5027.

Wieland, F. and Reimold, W.U., Field and Laboratory Studies on Shatter Cones in the Vredefort Dome, South Africa, and Their Genesis, *Met. Plan. Sci.*, 2003, vol. 38 (Suppl.), p. 5016.

Wu, J., Milkereit, B., and Boerner, D.E., Seismic Imaging of the Enigmatic Sudbury Structure, *J. Geophys. Res.*, 1995, vol. 100, pp. 4117–4130.

Wünnemann, K. and Ivanov, B.A., Numerical Modelling of the Impact Crater Depth-Diameter Dependence in An Acoustically Fluidized Target, *Planet. Space Sci.*, 2003, vol. 51, pp. 831–845.

Zharkov, V.N. and Kalinin, V.A., *Uravneniya sostoyaniya tverdykh tel pri vysokikh davleniyakh i temperaturakh*, Moscow: Nauka, 1968. Translated under the title *Equations of State for Solids at High Pressures and Temperatures*, New York: Consultants Bureau, 1971.

Zeldovich, Ya.B. and Raizer, Yu.P., *Fizika Udarnykh Voln i Vysokotemperaturnykh Gidrodinamicheskikh Yavlenii*, Moscow: Nauka, 1966. Translated under the title *Physics of Shock Waves and High-Temperature Hydrodynamic Phenomena*, New York: Academic Press, 1967.